



UNIVERSITY OF THE
WITWATERSRAND,
JOHANNESBURG

Rapid location detection of earthquake victims that are trapped beneath rubble in Haiti

Course Code: MECN4005A

Course: Design Project

Supervisor: Dr Chioniso Kuchwa-Dube

Course Coordinator: Mr Michael F Boer

A project report submitted to the Faculty of Engineering and the Built Environment, University of the Witwatersrand, Johannesburg, in partial fulfilment of the requirements for the degree of Bachelor of Science in Engineering.

Johannesburg, 7 September 2023

Executive summary

Earthquake prevention is not possible. The country of Haiti will always remain susceptible to earthquakes due to their geographical location at the boundary of tectonic plates. It is therefore vital to be prepared for the devastating impacts in the aftermath of earthquakes in Haiti. Earthquake search and rescue operations are often conducted in stages depending on the number of available personnel. The problem is obtaining the precise location of earthquake victims that are trapped beneath rubble. It is difficult for rescuers to traverse the affected regions due to the instability of rubble from collapsed infrastructure. Infrastructure in Haiti are built on land. As a result, a terrestrial design to solve the problem is not possible due to the unpredictability of the rubble stability. Marine designs do not possess the capability to traverse the land and hillsides. Hence, terrestrial and marine designs suffer from inaccessibility issues when attempting to solve the problem. To solve the problem, an aeronautical design was developed. The aeronautical design was achievable because it was able to perform non-contact data acquisition from an altitude above the disaster-stricken region. The solution comprised an unmanned aerial vehicle to navigate the affected regions and a combination of thermal camera modules to detect and identify victims trapped beneath rubble. This was a non-contact method and the stability of rubble did not require investigation to begin utilising the design, thus saving critical time. The thermal camera modules were integrated into the aircraft by the design of a mount. The mount permitted secure fitment of the cameras onto the aircraft while allowing camera wiring to be routed safely. The integrated design was fitted with a conventional tail configuration with a wing as the primary source of lift generation. The design was powered by a 175 kg turboprop engine with a power output of 900 HP. The engine functioned in a pusher configuration at the rear of the fuselage. The mission profile required the design to cover an area of $10\,459\text{ km}^2$ in 24 hours. The design was able to complete the mission in 21 hours with additional fuel that accounted for 53 nautical miles of loitering, if required.

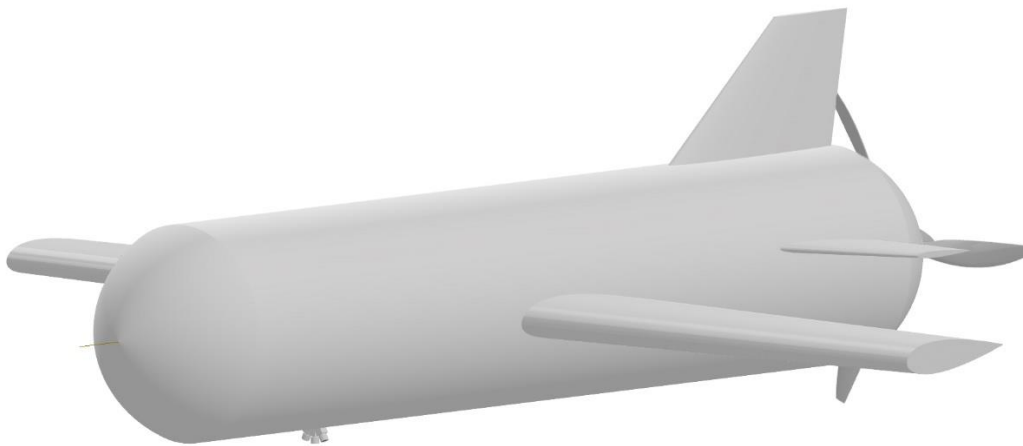


Figure 1 CAD model of the final integrated solution

Declaration sheet

List of content

Executive summary	i
Declaration sheet.....	ii
List of content	iii
List of figures.....	v
List of tables.....	vi
Nomenclature.....	vii
1. Problem analysis	1
1.1 Identification and background to the problem	1
1.2 Destructive problem analysis	3
1.3 Market survey	4
1.4 Identification of users.....	5
1.5 Functional analysis and final detailed problem analysis	5
2. Design considerations	7
2.1 Ability to detect victims beneath rubble	7
2.2 Weather	7
2.3 Detecting range	8
2.4 Detection region.....	8
2.5 Search pattern.....	10
2.6 Manned versus unmanned.....	10
3. Summary of the problem.....	11
4. User requirement specifications.....	12
4.1 Requirements	12
4.2 Constraints	12
4.3 Criteria	12
5. Design development.....	13
5.1 FLIR Lepton 3.5.....	13
5.2 ICI IR Inspector UAV Payload.....	14
5.3 ICI SWIR 640 P-Series	14
6. Design integration.....	42
7. Design specifications	45
8. Critical assessment of design	48
8.1 Operating cost	48
8.2 Recommendations for further work	49
9. References.....	50

10. Appendices.....	54
10.1 Appendix A.....	54
10.2 Appendix B.....	57
10.3 Appendix C.....	57

List of figures

Figure 1 CAD model of the final integrated solution	i
Figure 2 Number of earthquakes worldwide categorised by year [3]	1
Figure 3 Deadliest earthquakes worldwide since 1900 [4]	2
Figure 4 History of earthquakes in Haiti [6]	2
Figure 5 Average monthly temperatures in Haiti [9]	7
Figure 6 Map of Haiti showing the perceived shaking intensity caused by the earthquake in 2010 [11]	8
Figure 7 Comparison of distance from epicentre to outermost regions with strong shaking for various earthquakes in Haiti	9
Figure 8 Map of Haiti showing the population density [12]	9
Figure 9 FLIR Lepton 3.5 thermal camera module [14]	14
Figure 10 ICI IR Inspector UAV Payload system [15]	14
Figure 11 ICI SWIR 640 P-Series camera [16]	15
Figure 12 A visual representation of the Johnson Criteria	18
Figure 13 Graph showing the effect of operating distance on actual footprint distance	19
Figure 14 Schematic of ground sampling distance covered from the thermal camera at optimal operating distance [19]	20
Figure 15 Effective ground area covered by the thermal camera at 1620.98 metres above ground level	22
Figure 16 Affected region with collapsed infrastructure due to the 2010 earthquake in Haiti [21]	22
Figure 17 Ground width covered by three thermal cameras at 5 085.3 ft above ground level	23
Figure 18 Creeping line search pattern adapted to the affected regions in Haiti [21]	24
Figure 19 Final adapted creeping line search pattern [21]	24
Figure 20 Adapted sector search pattern [21]	25
Figure 21 Adapted expanding spiral search pattern [21]	25
Figure 22 Mission profile for the design	26
Figure 23 Effect of the design's wing aspect ratio on maximum lift-to-drag ratio	28
Figure 24 NACA 23024 airfoil profile [28]	29
Figure 25 Discretisations for each wing configuration	30
Figure 26 Effect of wing taper ratio on lift distribution	31
Figure 27 3D model of the wing	32
Figure 28 3D model of the horizontal tail	33
Figure 29 3D model of the vertical wing	34
Figure 30 3D model of the fuselage	35
Figure 31 Thrust comparison of engines at cruise altitude	36
Figure 32 3D model of translucent fuselage with integrated turboprop engine and propeller	37
Figure 33 Cross-section of the fuselage	38
Figure 34 Parallel search legs joined by manoeuvre points [21]	38
Figure 35 Interpretation for the turn manoeuvre performed by the design	39
Figure 36 Location of take-off and landing airports utilised by the design	40
Figure 37 Field performance for the design	40
Figure 38 Adjacent arrangement of thermal cameras	42
Figure 39 Triangular arrangement of thermal cameras	43
Figure 40 Conjoined arrangement of thermal cameras	43
Figure 41 Camera configuration with annotated dimensions	44
Figure 42 Annotated 3D view of the designed mount	44
Figure 43 Schematic of integration of cameras, mount and fuselage	45
Figure 44 Impact map for the 2018 earthquake used to plot Figure 7	54
Figure 45 Impact map for the 2021 earthquake used to plot Figure 7	54

Figure 46 Impact map for the 2022 earthquake used to plot Figure 7	55
--	----

List of tables

Table 1 Johnson's Criteria for thermal cameras [17].....	16
Table 2 Comparison of calculated thermal camera parameters	17
Table 3 Mass estimation data for the design.....	27
Table 4 Effect of the design's wing aspect ratio on maximum lift-to-drag ratio.....	28
Table 5 NACA 23024 airfoil properties [27].....	29
Table 6 Tornado input parameters used to obtain lift distribution.....	30
Table 7 Wing geometry for the design.....	32
Table 8 Horizontal tail geometry for the design	33
Table 9 Vertical tail geometry for the design	34
Table 10 Comparison of potential engines for the design.....	36
Table 11 Summary of performance specifications for integrated design.....	46
Table 12 Data used to plot Figure 13.....	57
Table 13 Bookkeeping drag table for the design	57

Nomenclature

μ_P	-	Propeller efficiency
ω	-	Turn rate
C_D	-	Drag coefficient
C_{D_0}	-	Zero-lift drag coefficient
C_L	-	Lift coefficient
C_{L_T}	-	Lift coefficient of tail
$C_{M_{CG}}$	-	Pitching moment coefficient about centre of mass
C_{M_0}	-	Zero-lift pitching moment coefficient
C_P	-	Power coefficient
C_R	-	Root chord
C_T	-	Tip chord
HP	-	Horsepower
L_{HT}	-	Tail arm to horizontal tail
L_{VT}	-	Tail arm to vertical tail
MAC	-	Mean aerodynamic chord
MALE	-	Medium altitude, long endurance
MTOW	-	Maximum take-off weight
n	-	Load factor
NACA	-	National Advisory Committee for Aeronautics
SFC	-	Specific fuel consumption
S_{HT}	-	Horizontal tail area
S_{VT}	-	Vertical tail area
V_{HT}	-	Horizontal tail volume coefficient
V_S	-	Stall speed
UAV	-	Unmanned aerial vehicle

1. Problem analysis

1.1 Identification and background to the problem

Earthquakes are among the most formidable and hazardous natural disasters that continually shape the geology of Earth. They are often described as sudden shaking or trembling of the ground caused by the release of accumulated energy in the Earth's crust. Earthquakes have captivated the attention of scientists and engineers for centuries due to their devastating impacts yet unpredictable nature. These seismic events occur worldwide at an approximate rate of 20 000 per year, affecting both developed and developing regions, leaving behind a trail of destruction and human suffering. [1]

Although many seismological institutions study earthquake patterns and are actively involved in earthquake prediction research, the aftermath of earthquakes remain catastrophic. Seismological institutions, such as United States Geological Survey, merely attempt to predict the seismic events and are able to implement early warning systems. They are not able to prevent the seismic activities. Consequently, there is often damaged infrastructure and loss of human lives.

Despite the absence of an upper limit on the Richter scale, earthquakes with a magnitude of five and above on the scale typically result in damage to infrastructure and/or human suffering [2]. Figure 2 shows the worldwide occurrence of earthquakes with a Richter scale magnitude of five or higher from 2000 to 2021. There was no precise trend but it must be noted that the graph did not distinctively diminish over time. This suggested ongoing seismic activity worldwide.

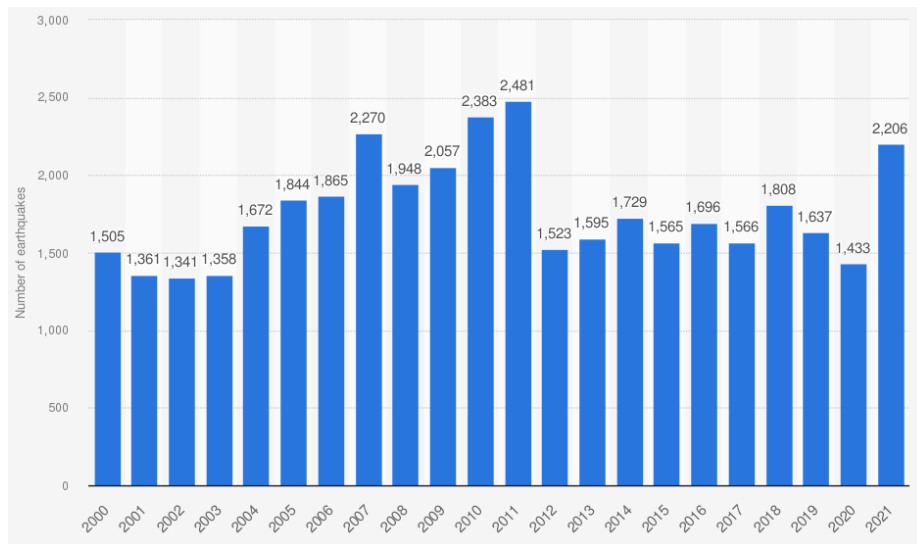


Figure 2 Number of earthquakes worldwide categorised by year [3]

The Richter scale magnitude serves as a metric for quantifying the intensity of an earthquake. Hence, a larger Richter scale magnitude earthquake results in more catastrophe. The Richter scale is limited in accurately measuring very large earthquakes. As the Richter scale magnitude increases, the scale's

accuracy diminishes, making it less suitable for earthquakes with magnitudes above a threshold of magnitude nine. However, the Richter scale served as a suitable measure for the purposes of this project.

Figure 3 shows the earthquakes since 1900 which resulted in the most deaths. The earthquake locations are included for reference.

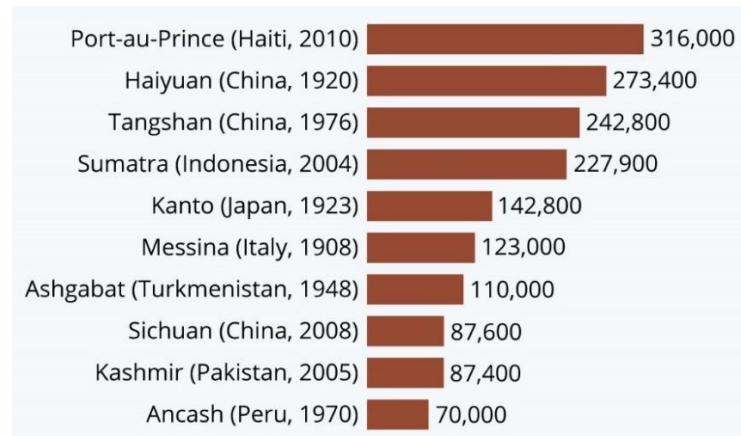


Figure 3 Deadliest earthquakes worldwide since 1900 [4]

From Figure 3, the recent earthquake that occurred in 2010 in Port-au-Prince, Haiti resulted in 316 000 deaths. This number was considerably large. The only earthquake that resulted in a higher death toll occurred in Shaanxi, China in 1556 with an estimated death toll of 830 000. The earthquake in 2010 in Haiti was evidence that an earthquake warning system was not fully adequate to prevent human suffering in the aftermath of the disaster.

Haiti has a history of earthquakes dating back to at least 1953, shown in Figure 4. Haiti is positioned at the northern boundary of the Caribbean Plate, where it interacts with the North American Plate through a plate boundary [5]. The North American Plate is shifting westward, but this movement is not continuous and results in friction with the Caribbean Plate. As a result, pressure accumulates between the two plates until it is eventually released in the form of an earthquake in the Haiti region. This geological evidence shows that Haiti will continue to remain vulnerable to earthquakes.

Date	Region	Depth	Magnitude	Deaths	Total damage
01/25/1953	Haiti		5.7	2	
03/02/1994	Saint-Louis Du Nord	3 km	5.4	4	
01/12/2010	Port-Au-Prince	10 km	7.0	316000	
10/07/2018	Port-Dex-Paix	24 km	5.9	18	
08/14/2021	Haiti	10 km	7.2	2248	
01/24/2022	Nippes	10 km	5.3	2	
06/06/2023	Haiti	9 km	4.9	4	

Figure 4 History of earthquakes in Haiti [6]

Due to the relatively shallow depth of earthquakes in Haiti, the effect felt on the surface of the Earth is often severe. This causes devastating damage to infrastructure in Haiti, resulting in an increased number of human lives lost.

Since the seismic activity in Haiti will likely not stop due to the geographical location, the issue of medics and rescue operations should be adhered to in the most efficient and timely manner. Search and rescue operations first conduct a comprehensive evaluation of the impacted area. This is done aerially or terrestrially to locate potential resources, hazards, and primary objectives for search and rescue teams. Subsequently, the impacted region is often divided into sectors to facilitate deployment of search teams.

Once search teams are deployed, they carry out swift search operations to maximize life-saving opportunities [7]. This is a vital stage of the search and rescue operation as the main goal of the team is to rescue as much victims as possible. The earthquake victims are either deceased or alive, some of which may be trapped beneath rubble. It is difficult to locate and assess the victims trapped under rubble.

The rescue teams need to be able to locate trapped survivors and assess who to rescue first based on their injuries to maximise the number of saved lives. Although trapped victims can survive up to a week under best circumstances, they still need to be located and assessed quickly and efficiently by rescue teams [8].

Locating the trapped survivors is a tough mission on its own. Once they are located, they need to be assessed and medically stabilised, if necessary. An incorrect location may cause further damage and harm to survivors due to wastage of time. The location of the trapped survivors needs to be accurate before medical assessments begin. Detecting the location of trapped survivors is done in stages and it often takes multiple stages before survivors deeply trapped beneath rubble are found. The problem is obtaining the accurate location of victims that are trapped beneath rubble and require medical attention.

1.2 Destructive problem analysis

From a high level, rescuers face challenges in accessing all areas where survivors might be trapped due to the presence of unstable debris and restricted visibility. In the aftermath of an earthquake, buildings and structures may collapse, leaving a chaotic landscape of debris. The debris can consist of concrete, metal, wood, and other materials, forming unstable piles that are difficult to navigate. The risk of secondary collapses or shifting debris further complicates rescue efforts, as rescuers need to exercise caution to avoid putting themselves in harm's way.

Locating survivors is a challenging task due to difficulty in detecting faint sounds or vibrations from survivors. The chaotic environment in disaster-stricken areas makes it difficult for rescue teams to identify potential survivor locations swiftly. Improved technology, specialized equipment, and well-coordinated search efforts are essential to increase the efficiency of the rescue operation and maximize life-saving opportunities in this critical and time-sensitive task.

The initial hours following an earthquake are of utmost importance, as the chances of survival decrease rapidly with time due to lack of food and water for the victims. Delays in accessing and reaching trapped individuals can significantly diminish the likelihood of successful rescues. As time elapses, survivors may face dehydration, injuries, or lack of oxygen, increasing their vulnerability and reducing their ability to withstand the harsh conditions. Hence, the rescue operation is extremely time-sensitive and vital to maximize the number of saved lives.

The issue of limited resources, encompassing personnel, equipment, and supplies, poses significant challenges to rescue operations during the earthquakes in Haiti. With disasters often striking unexpectedly and affecting vast areas, the demand for rescue efforts can quickly exceed available resources. Insufficient personnel may hinder the deployment of search and rescue teams to all affected locations, leading to delayed response times and leaving some areas underserved. Moreover, the scarcity of specialized equipment necessary for search and extrication can impede the effectiveness of rescue operations. Inadequate supplies, including medical resources and life-saving tools, further strain the ability to provide immediate assistance to survivors.

The task of distinguishing between earthquake survivors and non-survivors, presents a multifaceted challenge with emotional and practical implications. In disaster-stricken areas, rescue teams often encounter scenarios where individuals may be buried under debris, and the initial assessment may not reveal their condition. Determining whether someone is alive or deceased requires careful and thorough evaluation, involving visual observations, listening for faint sounds or signs of life, and possibly employing specialized technology such as thermal imaging to detect body heat. This process can be emotionally strenuous for rescuers, as they must confront the distressing reality of loss and survival while working in high-stress conditions.

1.3 Market survey

There are many methods in use for obtaining the location of victims trapped beneath rubble. However, they are not perfect and are subject to many factors.

- Helicopters are utilised in the first stage of search and rescue to give a vantage point over the disaster-stricken region. Although it provides a birds-eye view of the area it can merely be used for assessing the area for physical damage. Furthermore, utilisation of helicopters brings more noise and affects the ability to hear for trapped survivors. There is also an aerodynamic downwash effect from the helicopter. This means that the helicopter would need to maintain a minimum altitude to prevent any further damage due to the downwash effect.
- Canine rescue teams make use of dogs. The dogs are able to locate humans by sniffing their scent in a region. This method quickly becomes ineffective because the dogs get tired and often need to be rotated to maintain efficiency. Wind affects their scent and may lead to an incorrect

location in rubble. Hence, the effectiveness of canine rescue teams is largely dependent on the weather conditions and size of the affected region.

- Rescuers manually check for voids in the rubble. The effectiveness of this method is dependent on the number of dispatched rescuers and the size of the affected area. Rescuers often get tired and will need to be rotated once fatigue settles in. The method works on the premise that if a victim is in a large void, then they will have more space to manoeuvre while smaller voids will result in less space to move.
- Workers listen for sound from victims. This is difficult because a quiet environment is required to effectively distinguish the sound of trapped survivors. Adverse weather conditions such as wind and rain may affect the ability to listen for survivors.
- Advanced equipment such as heartbeat sensors, carbon dioxide detectors, and thermal imaging devices are used to detect humans beneath rubble. Ground-penetrating radar is sometimes also used to detect voids where victims may be without physically excavating to check. These methods are employed by ground teams. Their effectiveness depends on the stability of debris, accessibility to the affected region and unknown hazards such as gas leaks and live electrical wires.

The viability of each method depends on the circumstances in the situation such as availability of resources, level of expertise available, time elapsed since the earthquake, and the depth of the rubble.

1.4 Identification of users

The users of the design will essentially be search and rescue teams in Haiti. Humanitarian organisations such as the UN, UNICEF, and Red Cross may also make use of the design as their intention is to save human lives following natural disasters. The government in Haiti may opt to use the design since they are fully aware of the risk that Haiti faces with possible earthquakes in the future due to the geographic location of Haiti.

1.5 Functional analysis and final detailed problem analysis

Many challenges inherently exist with locating trapped earthquake survivors beneath rubble, especially at great depths below the surface. These challenges remain key to developing a design that will solve the problem efficiently.

The problem is to accurately locate survivors that are trapped beneath rubble. If the design cannot perform this function, it will be, at best, a non-optimal solution. The design will be utilised by search and rescue teams whose main goal is to save lives amidst the aftermath of the earthquake.

The weather conditions pose a significant risk to the search and rescue operation. Adverse weather conditions such as rain or hail have the potential to delay the rescue procedure. Hence, the design should

be able to operate under all weather conditions following the earthquake. Various weather conditions should not affect the reliability and efficiency of the design.

The search and rescue procedure is a time-sensitive operation. It is vital for the design to locate all trapped survivors in the disaster-stricken area within 24 hours. After 24 hours, the chances of survival for trapped humans drastically diminishes with time. [8]

The application of the design will be, in most cases, unexpected. If an earthquake occurs swiftly the design must be readily available to ensure that the number of saved lives is maximised. Given the size and dense population of Haiti, the design must be able to deploy or utilise immediately to cover maximum ground in minimum time. There should be no waiting period to use the design because human lives are at stake. These challenges should be resolved by the design in order to ensure a successful, optimised solution.

The problem lies in the intricate and time-sensitive task of detecting the precise location of earthquake survivors trapped beneath rubble during a rescue operation, as rescuers must navigate through unstable debris difficulties in discerning faint survivor signals, all within a critical time window, to maximize life-saving opportunities and minimize the risk of further harm to victims.

2. Design considerations

The exact devastating impact of earthquakes is unpredictable. It is not known which buildings will collapse and how many humans will be trapped under rubble. As a result, it is important to develop a successful design that is capable of operating under the worst conditions after an earthquake has occurred. Since the focus of the design is to locate trapped victims, the feasibility of the design to operate in unaffected regions must be considered.

2.1 Ability to detect victims beneath rubble

The design should possess the capability to detect humans trapped beneath rubble. The design should be able to distinguish a human from other life forms and objects. This is a vital consideration of the design as it will decide whether the design is adequate for the mission or not. The means by which the design detects the human is not restricted.

2.2 Weather

Earthquakes do not occur seasonally. They can occur suddenly at any moment. The design must be able to operate under all weather conditions at optimal efficiency. Based on past data shown in Figure 5, Haiti experiences an average maximum and minimum temperature of 31.55°C and 22.04°C, respectively.

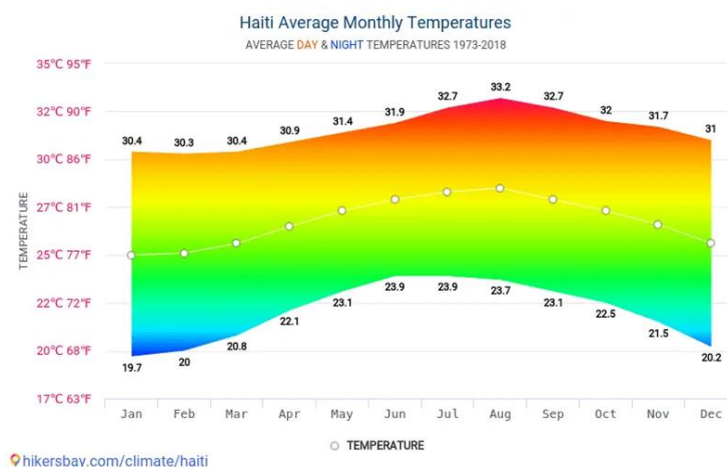


Figure 5 Average monthly temperatures in Haiti [9]

Haiti experiences a tropical climate with variable rainfall from April to November during rainy season [10]. These variations in climate must not affect the capability and mission performance of the design. The design should operate optimally when rainfall occurs. Furthermore, the design must be able to operate at all times of the day. This will ensure that trapped victims are not only located during a designated time or period since earthquakes can occur at any time of day.

2.3 Detecting range

The design's operating detection range must be considered. A design that has a maximum detecting range that is smaller than the depth of the rubble will have reduced mission performance. This is because it will be insufficient to detect humans at large depths beneath the rubble. Rescue teams will need to remove multiple layers of rubble to reduce the rubble depth in order for the design to detect these humans. A design that is able to perform a single detection of humans at all depths will have better mission performance. Rescue teams will know exactly where to remove rubble to prevent further harm or damage.

2.4 Detection region

The design's use case must be established. The region and parameters such as population density and area coverage must be recognized. The deadly earthquake that occurred in 2010 in Haiti had a 7.0 magnitude on the Richter scale. The impact of the earthquake is shown in Figure 6.

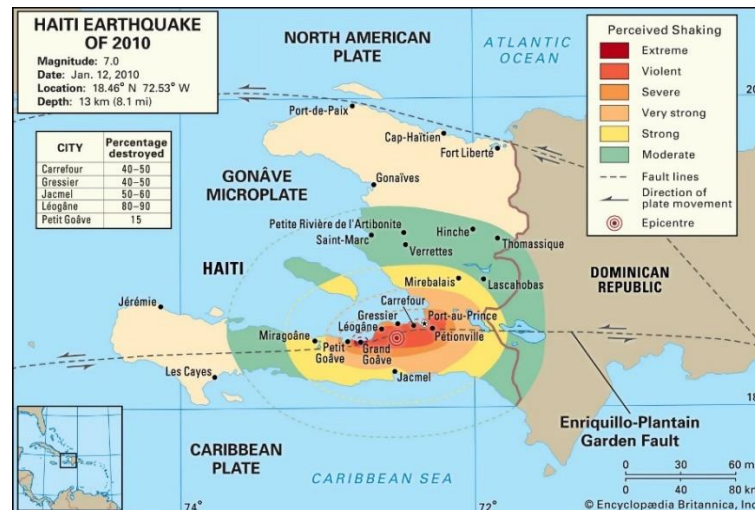


Figure 6 Map of Haiti showing the perceived shaking intensity caused by the earthquake in 2010 [11]

From Figure 6, the impacted areas with perceived shaking ranging from strong to extreme were measured. It was noted that these impacted regions made up a circle of radius 57.7 km from the epicentre of the earthquake. The same method was conducted using the mapped impacted regions from the earthquakes that occurred in Haiti in 2022, 2021, and 2018. This was done to identify a trend in the distance from the impacted regions with collapsed infrastructure to the epicentre. Figure 7 compares the radius of a circle extending from the epicentre to the outermost regions which experience infrastructure collapse or strong shaking for the earthquakes that occurred in 2010, 2018, 2021 and 2022 in Haiti. The impact maps used to generate Figure 7 are available in Appendix A.

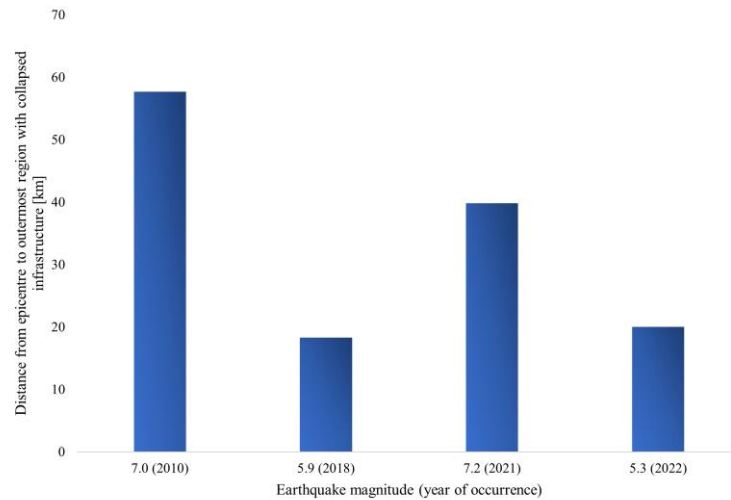


Figure 7 Comparison of distance from epicentre to outermost regions with strong shaking for various earthquakes in Haiti

From Figure 7, there was no correlation between the Richter scale magnitude of the earthquake and the distance from the epicentre to the outermost region. Although the 2021 earthquake had a higher Richter scale magnitude than the 2010 earthquake, the distance from the epicentre to the impacted regions was lower.

The design must be capable of completing a mission that covers the “circle of impact”. The worst-case scenario for this occurred in 2010 with the circle having a radius of 57.7 km, as shown in Figure 6. In 2010, the earthquake epicentre was at Port-au-Prince. This is the capital of Haiti and the city with the largest population. A map of the population density in Haiti is shown in Figure 8. This effectively depicts which areas are at higher risks for victims to be trapped beneath rubble.

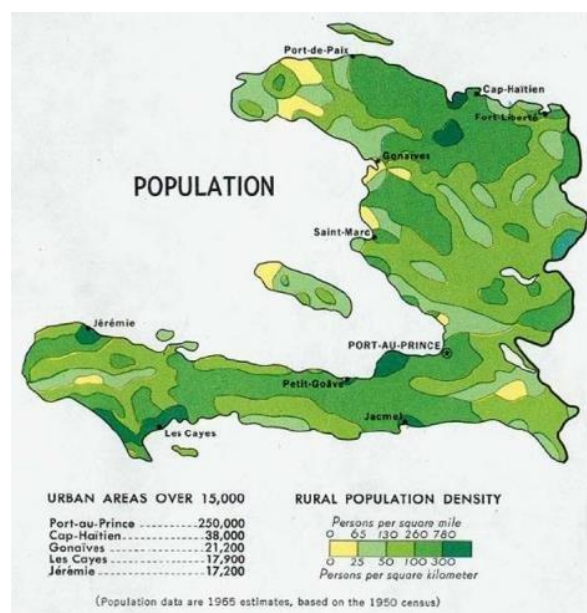


Figure 8 Map of Haiti showing the population density [12]

According to the population distribution in Figure 8, Port-au-Prince has a 557.9% increase in population over Cap-Haitien. It was therefore established that the earthquake which occurred in 2010 was likely the worst-case scenario since the epicentre coincided with the most populous city in Haiti. This resulted in thousands of victims trapped beneath rubble. The effects of an earthquake with the same magnitude but with an epicentre at a sparsely populated region would be much lower. Hence, it is sensible for the design to be capable of operating over the impacted regions of the 2010 earthquake. It must be considered that the design will be able to detect victims over these affected regions.

2.5 Search pattern

The design will likely need to traverse the impact region to detect trapped victims in the entire region. The direction of traversal or search pattern will be explored. This will directly affect the mission profile of the design. It will also affect the time taken to complete the mission as duplicate scans of the same portion of region will consume time.

2.6 Manned versus unmanned

Since the design will require traversal in some, there is control involved. The feasibility of a manned versus unmanned design must be considered. The advantages and disadvantages of both approaches will be compared to determine the effect on the mission profile and design parameters such as mass.

3. Summary of the problem

Haiti, a country in the Caribbean, will always remain prone to earthquakes due to their geological location. Since the severity of these earthquakes is not known, the aftermath cannot be predicted. The problem exists with the search and rescue teams locating victims that are trapped beneath rubble. SAR teams are unable to prioritise who to rescue first as they do not know where the trapped victims are. A solution is required that will enable search and rescue teams to detect the location of trapped victims without causing further harm to them. Consequently, search and rescue teams will be able to make an informed decision on prioritisation of medical treatment. This will give them the potential to maximise the number of lives saved.

4. User requirement specifications

4.1 Requirements

- The solution must be able to detect human life forms through rubble.
- The solution must be capable of detecting humans in all weather conditions.
- The design must permit the capability to scan the entire disaster-stricken region.

4.2 Constraints

- The detail or resolution of the detection method may affect the accuracy of the solution, which in turn may affect the ability to discern the medical state of the victim.
- The unpredictability of weather conditions and stability of rubble may affect the mission performance of the design.

4.3 Criteria

- The ratio $\frac{range}{duration}$ must be as high as possible to ensure that the design maximises the range to cover the disaster-stricken region while minimising the duration to cover the region.

5. Design development

The technique of detecting humans through multiple layers of solid building material was difficult. The method must be accurate and capable of differentiating human life forms from inanimate objects. Research was done on potential devices that enabled the user to effectively “see” through multiple layers of rubble.

Listening devices such as seismic sensors could be deployed to detect faint sounds from survivors. Seismic sensors are very sensitive and are able to detect slight noises that may be coming from trapped survivors. An immediate downfall to these devices was that footsteps from search and rescue teams, inclement weather conditions and distress calls would be detected by the device, hindering its accuracy. In order for the device to be effective, a specialized user would then need to filter out unwanted signals to focus on potential signals from trapped victims. This process would consume more time and need to be done several times across the disaster-stricken area depending on the detection range of the seismic sensor. Since seismic sensors are based on the principle of sound waves, trapped unconscious victims may not be detected. Furthermore, victims that are alive but not creating any sound may not be located. This results in the use of seismic sensors as partially efficient. The sensors only have the potential of locating trapped victims that emit noise like movements, shouting, and crying. Depending solely on the use of seismic sensors to solve the problem will essentially result in an ineffective solution.

Thermal imaging devices may be utilised to capture heat signatures given off by humans beneath the rubble. These devices work based on the principle of capturing the infrared radiation emitted by objects, including humans, which may allow rescuers to identify temperature variations and locate potential victims. A thermal imaging device also assists in detection through smoke, dust and all weather conditions. This method may be advantageous over the use of listening devices as it is capable of detecting humans through heat signatures even if they do not make a noise. The method of thermal imaging is a non-contact method of detection. This ensures that survivors are not further harmed during the location detection phase. The technique of thermal imaging was explored as a potential device to locate trapped victims as a solution.

Three potential infrared cameras were identified and compared for use in detecting trapped victims. The cameras were:

5.1 FLIR Lepton 3.5

This was a thermal imaging camera that could measure temperature with precision and was compatible with various devices. The camera came with focal plane arrays offering 160x120 active pixels. Notably, the radiometric Lepton was able to provide accurate and calibrated temperature data for each pixel in every captured image, making it a potentially versatile and valuable tool for locating trapped victims [13]. The FLIR Lepton 3.5 was shown in Figure 9.



Figure 9 FLIR Lepton 3.5 thermal camera module [14]

5.2 ICI IR Inspector UAV Payload

This system integrated the 8640 USB camera with a high-resolution visible camera from the Sony R10C, enabling remote asset inspection and identification. Both cameras came with remote electronic focus and zoom capabilities, offering a narrow horizontal field of view of up to six degrees [15]. This versatile system, shown in Figure 10, was identified as potentially useful in the detection of trapped victims.



Figure 10 ICI IR Inspector UAV Payload system [15]

5.3 ICI SWIR 640 P-Series

The ICI SWIR infrared camera achieved remarkable sensitivity to energy within the near- and shortwave-infrared wavebands. This sensitivity surpassed the capabilities of silicon charge-coupled cameras by a considerable margin [16]. The lens for this camera was replaced with a SO-SWIR-1000-23 lens manufactured by Shanghai Optics. This lens was selected as it had a large focal length of 100 mm. A large focal length was desirable as it allowed high magnification and low image distortion. The ICI SWIR 640 P-Series camera was shown in Figure 11.



Figure 11 ICI SWIR 640 P-Series camera [16]

The use case for the thermal imaging camera was entirely dependent on the specifications of the device. Specifications such as the detection range inevitably dictated how the thermal camera should be implemented for maximum effectiveness. The important specifications for all three potential cameras were calculated and compared.

The target critical dimension was a vital parameter that was determined. It referred to the minimum size or resolution required to detect and measure temperature differences accurately and reliably. In the application of search and rescue operations, the safety of all humans had equal importance regardless of their age or size.

The thermal camera had to account for all humans, and so the critical dimension had to align with the size of a newborn baby. This ensured that the camera was able to detect the smallest human as the worst-case scenario, which was also applicable to any other human larger in size.

The target critical dimension was calculated based on the average width and height of a newborn baby using:

$$Target\ critical\ dimension = \sqrt{Target\ height * Target\ width} \ [m] \quad (1) [17]$$

Pixel IFOV (instantaneous field of view) essentially specified how much area each pixel on the camera could see. A smaller pixel IFOV indicated that each pixel on the camera could capture a smaller area, similar to having a higher number of pixels in an image. This increased level of detail enabled the camera to display more precise information and identify subtle changes in temperature.

The pixel IFOV for all thermal cameras was determined using:

$$Pixel\ IFOV = \frac{pixel\ pitch}{focal\ length} \ [mrad] \quad (2) [17]$$

PPM referred to the pixels per metre and was a measure of the number of pixels that covered a distance of one meter in the captured thermal image. PPM was a parameter that helped determine the level of detail and clarity in the thermal image. This assisted in detection and possibly identification of trapped victims.

PPM was calculated using:

$$PPM = \frac{2 * \text{number of required cycles from Johnson criteria}}{\text{Target critical dimension}} \left[\frac{\text{pixels}}{m} \right] \quad (3) [17]$$

The main objective of Johnson's Criteria was to determine the minimum level of performance required for a thermal imaging system to be useful for specific applications, in this case detection of trapped victims. Johnson's Criteria specified the number of cycles required for different purposes, shown in Table 1.

Table 1 Johnson's Criteria for thermal cameras [17]

Desired objective	Number of cycles required
Detection	0.75
Recognition	3
Identification	6

The operating range of the camera was important because it essentially affected how the camera was implemented (a stationary or moving design).

The operating range was determined using:

$$\text{Operating range} = \frac{1000}{PPM * \text{pixel IFOV}} [m] \quad (4) [17]$$

The operating range of the thermal camera was dependent on the PPM which was directly dependent on the desired objective from the Johnson Criteria. As a result, the desired objective from Table 1 affected the operating range of the thermal camera for the specific application.

The inputs for equations (1) to (4) are available in Appendix A. The results for the potential thermal cameras were shown in Table 2.

Table 2 Comparison of calculated thermal camera parameters

Parameter	FLIR Lepton 3.5	ICI IR Inspector UAV Payload	ICI SWIR 640 P- Series
Target critical dimension [m]	0.3317	0.3317	0.3317
Pixel IFOV [mrad]	6.78	0.49	0.17
PPM [$\frac{pixels}{m}$]	4.522	4.522	4.522
Operating range [m]	65.23	910.55	2601.57

Table 2 was based on the number of cycles required for detection. The ICI SWIR 640 P-Series thermal camera had a larger operating range than the FLIR Lepton 3.5 and ICI IR Inspector. This meant that the SWIR 640 P-Series was able to detect targets from a maximum distance of 2 601.57 metres while the Lepton 3.5 and IR Inspector operating range was only 65.23 and 910.55 metres, respectively. The SWIR 640 P-Series had the lowest pixel IFOV which meant that each pixel on the thermal camera captured a smaller area. This allowed for enhanced detail in the thermal image and showed that it was superior than the competitors in that aspect. Enhanced details assisted with confirmation of trapped victim detection as more pixels rendered a sharper, clearer thermal image.

The resolution for the ICI IR Inspector and SWIR 640 P-Series were both 640x512 while for the Lepton 3.5 it was 160x120 [15], [11]. This indicated that the IR Inspector and SWIR 640 P-Series were able to output a clearer image since the pixel resolution was greater than the Lepton 3.5 in both horizontal and vertical directions. It was evident that the ICI SWIR 640 P-Series was superior over the Lepton 3.5 and IR Inspector for use in the application of trapped victim detection.

According to the Johnson Criteria, a thermal camera was capable of detection, recognition and identification as shown in Table 1. The data in Table 2 was determined using the criterion for detection, however this was not enough for the search and rescue team. A detection did not necessarily mean that the heat signature was coming from a human. It could have been such that an object was emitting heat and met the target critical dimension according to the thermal camera.

For the purposes of search and rescue, an identification criterion sped up the operation. Rescuers did not need to figure out where the heat signature was coming from since the thermal image revealed an identifiable victim. The principle behind this was shown in Figure 12.

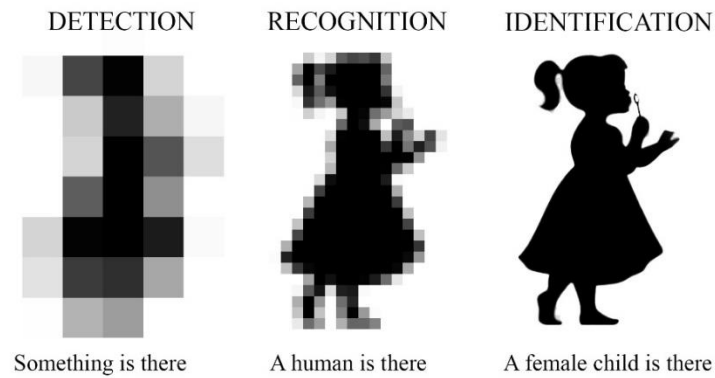


Figure 12 A visual representation of the Johnson Criteria

Due to the time-sensitive nature of the problem, it was critical that the design solved the problem in a timely manner to ensure a maximum number of saved lives. A design that was able to produce identifiable thermal images assisted search and rescue teams in quickly prioritizing who to rescue first based on injuries. Identifying targets helped rescuers notice victims' body language and movements, which assisted in knowing whether the victim was conscious, unconscious, or deceased.

Since the produced thermal image was clear enough for human identification, rescuers were able to discern the state (conscious, deceased, or unconscious) of the human through their body language. However, this might not always have been the case, as a conscious victim might not move due to being confined within the rubble. As a result, further measures had to be taken simultaneously to ensure that the state of the identified victim was known. This was vital for search and rescue teams to begin prioritization of medical resources and manpower to remove rubble.

Multiple methods could be employed. In the thermal images, rescuers had to be aware of the victims' eyes. Any body gestures or blinking effectively meant that the victim was conscious. Verbal communication was attempted by search and rescue teams in the region of the identified victim. If the victim responded verbally or through gestures, it indicated consciousness. Auditory cues such as breathing, coughing, or moaning also indicated consciousness of the victim. Rescuers had to be aware of this and avoid producing excessive noise to listen for audible signs.

It required approximately 12 hours for a human body to feel cool on the skin and about 24 hours for the body's core temperature to become lower than ambient temperature [18]. Depending on how much time elapsed since the earthquake, the identified human may have shown differently on the thermal image. Once the victim had been identified on the thermal image, the actual heat signature intensity must be noted. A colder heat signature alluded to the fact that the victim has deceased since their body temperature decreased over time after death. Rescuers had to take the heat intensity into account when identifying victims. However, these heat signatures could not be used to distinguish between consciousness and unconsciousness.

It was evident that additional measures had to be taken due to the multi-faceted nature of the problem. Search and rescue teams could not rely solely on the design to perform every aspect of identification as there were many factors to consider such as safety, stability of the rubble, and environmental noise.

The operating distance for the ICI SWIR 640 P-Series with a Shanghai Optics SO-SWIR-1000-23 lens was calculated using the Johnson Criteria for identification. It was found that the camera's maximum operating distance for identification of targets was 1625.98 meters. This meant that the thermal camera was capable of producing thermal images in which the victims were identifiable from a maximum distance of 1625.98 meters.

The ground sampling distance was calculated based on the camera's sensor width, pixel resolution and focal length. The operating distance was varied from 0 metres to a maximum of 1625.98 metres to determine the effect of operating distance on a single image footprint width and height. A buffer of 5 metres was used to allow the camera to operate effectively on potentially trapped victims 5 metres below the surface. The image footprint width and height had a direct impact on the number of images to be captured to cover the disaster-stricken region. The results were plotted and shown in Figure 13.

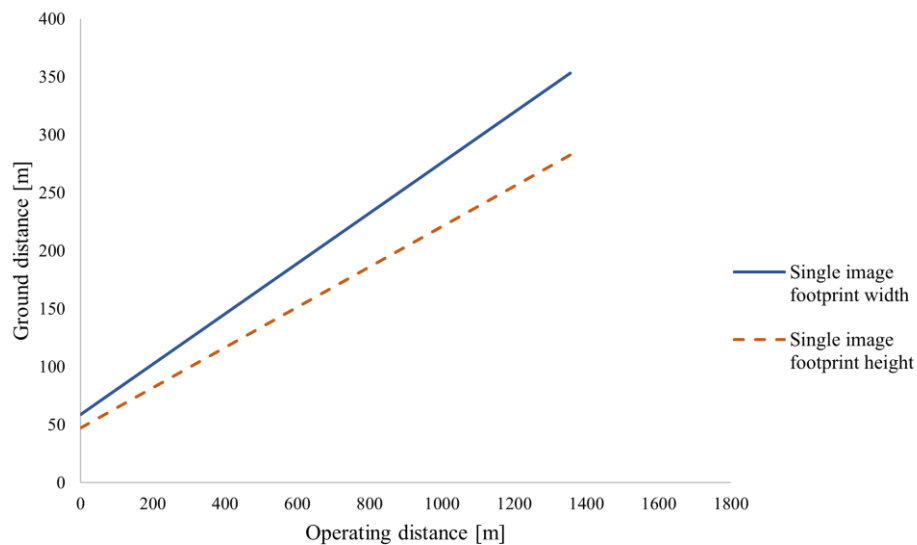


Figure 13 Graph showing the effect of operating distance on actual footprint distance

From Figure 13, it was noted that a larger operating distance resulted in more ground being covered. As a result, for the camera to have operated at maximum effectiveness (covering the most area in a single image footprint), it should have captured images at a distance of 1625 meters from the target. Ensuring that the camera captured the maximum area in a single image reduced the time taken to cover the disaster-stricken region. Hence, mission completion time was reduced and resulted in more lives being saved. The data used to plot Figure 13 is available in Appendix B.

A potential method to have ensured that the camera operated at a distance of 1625 meters from the surface was the use of a flying solution at an altitude of 1625 meters above the surface. A schematic of this analogy was shown in Figure 14.

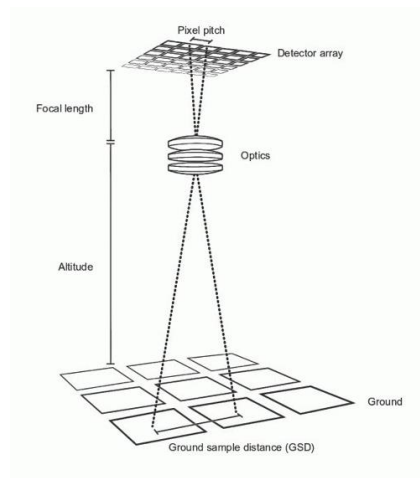


Figure 14 Schematic of ground sampling distance covered from the thermal camera at optimal operating distance [19]

The initial problem of detecting victims trapped beneath rubble was solved with the use of an ICI SWIR 640 P-Series camera with a Shanghai Optics SO-SWIR-1000-23 thermal lens. However, the camera was capable of detecting trapped victims with a caveat. The camera was only able to operate at maximum efficiency from an operating distance of 1625.98 metres. If the camera was utilised at a lower operating distance, then the area covered would be lower. It was therefore vital that the design had the capability to traverse the disaster-stricken region as a single image that covered an small area of was not enough.

The camera had a maximum operating distance of 1625.98 meters. It was therefore imperative for the design to maintain that distance from the target. An increase in distance would have resulted in the camera being unable to scan the target. A decrease in distance would have resulted in a smaller region being scanned. It was important for the design to constantly search the area while consistently maintaining the camera's maximum operating distance.

The viability of terrestrial, sea and air-based designs were investigated at a high level.

A sea-based design was inadequate. Navigating Haiti's terrain from the sea presented formidable challenges due to potential obstacles like cliffs, rocky outcrops, and dense shoreline vegetation, which hindered sea-based designs' access to disaster-prone regions. These designs, optimized for water operations, often lacked the mobility and terrain-crossing capabilities necessary for navigating the rough and debris-laden landscapes typical of earthquake-affected regions. Furthermore, their operational range and reach on the island were limited, especially when attempting to access its interior, potentially resulting in missed disaster regions and reduced coverage. Their operation at or near sea

level restricted their effectiveness in scanning elevated terrain, a significant concern in earthquake scenarios where victims might have been trapped beneath rubble in remote or elevated locations.

Island terrain such as Haiti's, marked by its diverse characteristics including steep slopes, dense forests, and challenging topography, has historically posed navigation challenges for land-based vehicles. These vehicles have encountered obstacles such as debris, collapsed structures, and other impediments, common in earthquake-affected areas, which could hinder their progress and potentially lead to mission failure. Similar to sea-based counterparts, land-based vehicles also faced limitations in range and accessibility, particularly when attempting to reach remote or isolated island areas. Moreover, operating land-based vehicles in unstable post-earthquake environments carried safety risks for operators, particularly in regions susceptible to landslides or aftershocks. Additionally, the stability of rubble is often not known until the first stage of search and rescue evaluation is completed. Deploying a land-based design only after waiting for clearance from the search and rescue team consumed valuable time and was therefore not ideal for the application.

Aerial designs offered several advantages for disaster response. Their mobility and accessibility allowed them to quickly navigate diverse and challenging terrain, including inaccessible areas, without hindrance from obstacles, rubble or rough terrain. Aerial designs provided an elevated perspective for capturing images and thermal data, making them ideal for surveying both ground-level and elevated regions like hillsides or cliffs. They could efficiently maintain a specific distance from the target, such as the required 1625 metres, by adjusting altitude and flight path, optimizing the thermal camera's image footprint. Operating from the air enhanced safety by reducing risks to human operators, particularly in hazardous post-earthquake environments, as designs could be controlled remotely from a secure location. Additionally, their quick deployment to disaster areas ensured timely assistance and enhanced the chances of locating survivors. As a result, an aerial high-level design was ideal to solve the problem.

Since the design operated aurally, the altitude had to be taken into account. It was ideal for the camera to operate 1625.98 meters from the target, corresponding to an identification region of 353.163 m x 282.53 m. However, a drawback to this distance was that the camera could only identify targets on the surface of the ground; any targets below ground level fell out of the camera's detection region. Hence, a buffer distance was imperative to identify targets below the surface and subsequently beneath rubble. A buffer distance of 5 meters was used as search and rescue teams still needed to perform rubble removal operations to reach the trapped victim. This meant that the aerial design operated at an altitude of 1620.98 meters above the surface of Haiti, covering a region with a width of 352.07 meters and a height of 281.66 meters. A visual representation of this was shown in Figure 15.

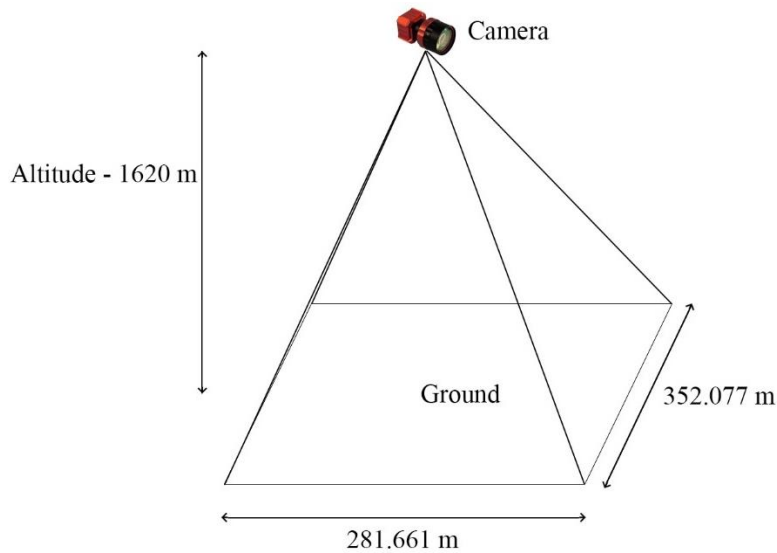


Figure 15 Effective ground area covered by the thermal camera at 1620.98 metres above ground level

At an altitude of 1620.98 metres above ground level, the camera covered a limited region. This meant that the design needed to possess mobile capabilities to allow the thermal camera to cover more ground.

Figure 16 showed the affected regions that experienced strong to intense shaking, resulting in collapse of infrastructure.



Figure 16 Affected region with collapsed infrastructure due to the 2010 earthquake in Haiti [21]

The size of the affected region shown in Figure 16 was $10\,459\text{ km}^2$. The effective ground area covered by the thermal camera was 0.0992 km^2 . It was evident that the camera ground coverage was miniscule when compared to the size of the search area. The search area could not change; therefore, the ground

coverage of the camera was reconsidered. Two more thermal cameras were added as a means to increase the ground coverage. The additional camera positions were adjusted to allow maximum ground coverage. This was done by tilting the additional cameras by 27.2 degrees in opposite directions to ensure that the cameras' FOV do not overlap and produce duplicate images. The effective ground coverage width was increased. The tilting of the additional cameras meant that the ground coverage was at an angle relative to the ground. Hence, the distance from the three cameras to the ground (altitude) had to decrease to account for this. The ground coverage of all cameras needed to be re-calculated due to the change in distance from the cameras to the target. The final changes were shown in Figure 17. The ground covered by all three cameras in a single image was 0.2805 km^2 . This was a 182.762% increase from the initial ground coverage of a single thermal camera.

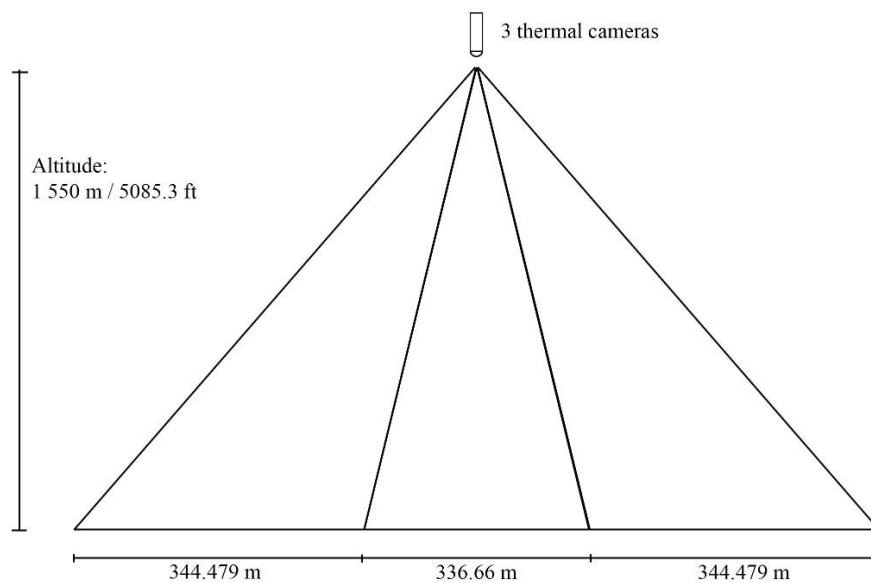


Figure 17 Ground width covered by three thermal cameras at 5 085.3 ft above ground level

The versatility of different search patterns was investigated. The creeping line search pattern was explored as a potential use for the design. The search pattern was adapted to the affected regions in the 2010 earthquake. This was shown in Figure 18.

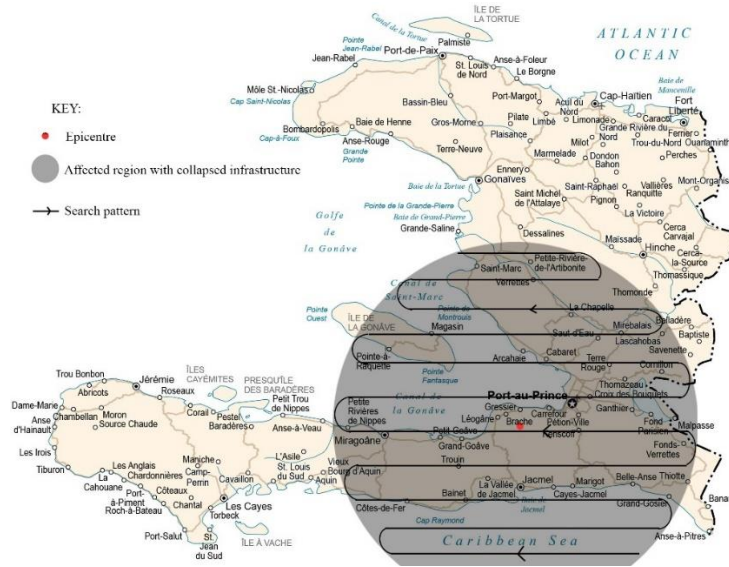


Figure 18 Creeping line search pattern adapted to the affected regions in Haiti [21]

The oceanic regions that did not require scanning were removed as there would be no trapped victims below rubble in those regions. At the end of every search leg, manoeuvring points were considered to allow the design to turn and perform the next search leg. The distance between each search leg was the total ground width of 1025.618 metres covered by the combination of thermal cameras. Figure 19 depicted the final adapted creeping line search pattern that was considered for the design.

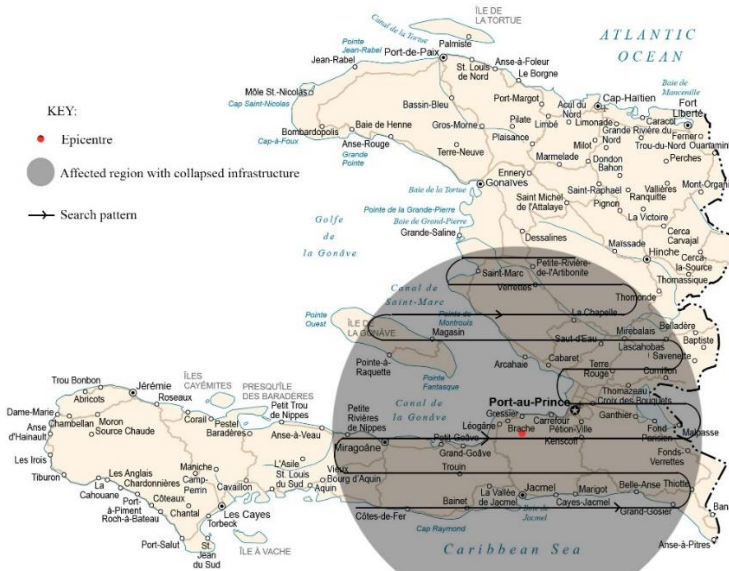


Figure 19 Final adapted creeping line search pattern [21]

The viability of a sector search pattern was also explored. This pattern traversed the region aerially in triangular sectors. However, it was noted that the manoeuvre points required more area than the adapted creeping line pattern and thus, increased mission duration. Due to the relatively small region of ground coverage, multiple triangular sections were required. This further increased the time taken to manoeuvre

and perform the next search leg. A schematic of this search pattern was shown in Figure 20. Coverage of oceanic regions were minimised as they did not require scanning. However, they were not avoidable.

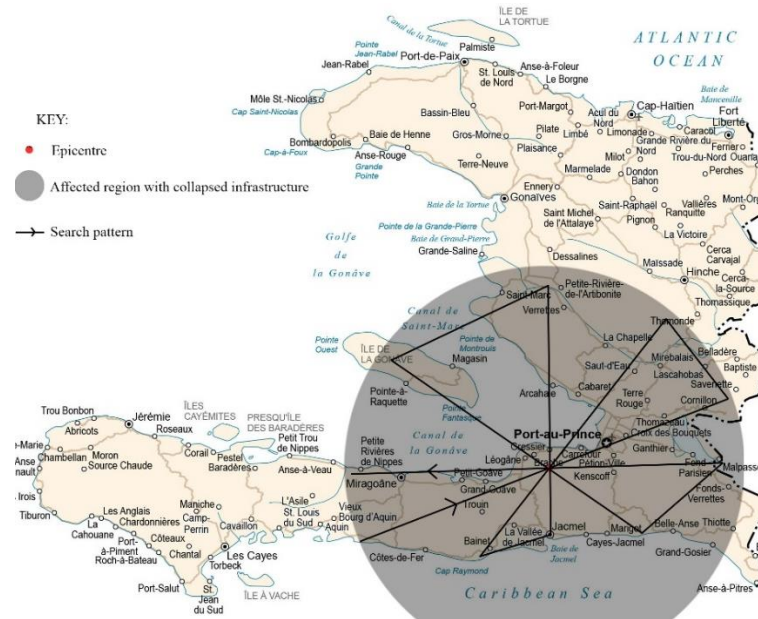


Figure 20 Adapted sector search pattern [21]

The expanding spiral search pattern was adapted to the affected region. The search began at the epicentre due to the region having more intense shaking than the surroundings. The search continued outward in an expanding spiral pattern. This was advantageous because it was likely that more fatal injuries occurred in regions closer to the epicentre. Due to the affected region mapped as a circle, the search pattern resembled an expanding spiral. The adapted expanding spiral search pattern was shown in Figure 21. Scans over oceanic regions was unavoidable due to the search pattern being a continuous spiral.

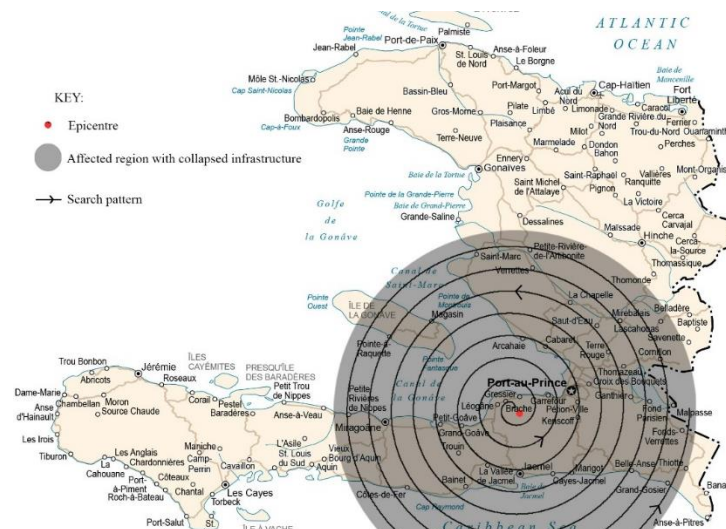


Figure 21 Adapted expanding spiral search pattern [21]

The adapted creeping line search pattern was selected over the adapted expanding spiral and sector search patterns due to its efficient and systematic coverage of the search area. It ensured complete coverage, optimized resource use for the design such as time and energy, maintained consistency while searching, and enabled easy tracking of progress. Unlike the adapted expanding spiral pattern that led to unnecessary scans over oceanic regions and the sector pattern that required excessive manoeuvring, the adapted creeping line approach offered a methodical and unduplicatable way to search for victims.

To traverse the country and conduct the search pattern, the design required propulsion. The feasibility of propulsion systems was explored. Jet engines were not ideal as the design was not required to travel as fast as possible. Furthermore, the noise generated by jet engines can be disruptive and may limit the ability to hear distress calls or signals from survivors on the ground. Rotary wings generated lift and propulsion and were commonly used in rotorcraft designs. However, the design must be able to achieve maximum range to cover the disaster-stricken region. Rotary wings were more vulnerable to adverse weather conditions, such as high winds and turbulence, which affect their safety and performance during long-range missions. Propeller propulsion was ideal for the design as it was suitable for low-speed flight, high endurance and good versatility, aiding the thermal camera with capturing images.

The mission profile for the design was developed. Using the ground distance covered by the camera in Figure 17, the number of required search legs were found and hence, the range for the mission was determined. The altitude for the mission was pre-determined using the operating distance of the combination of thermal cameras, obtained from Figure 17. The mission profile for the design was shown in Figure 22.

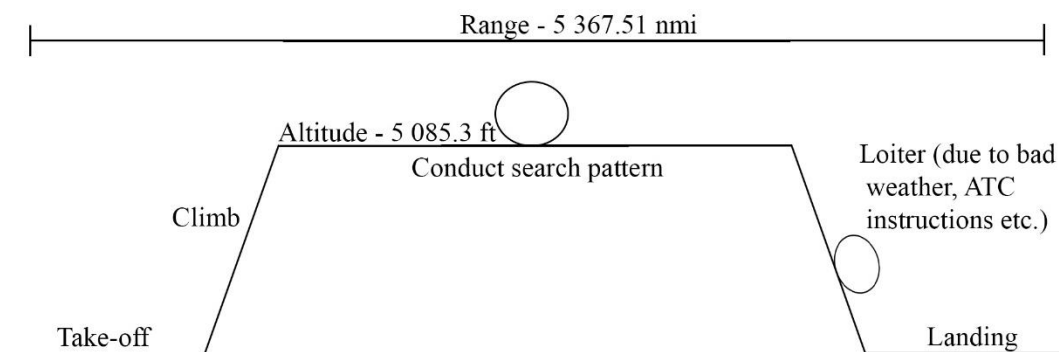


Figure 22 Mission profile for the design

Based on the mission profile shown in Figure 22, potential aircraft that were able to perform the mission was investigated. The most apt aircraft that could almost perform the mission in terms of the altitude and range was the Elbit Hermes 900. The Hermes 900 was a military MALE UAV that was designed to fulfil a range of tasks, including surveillance, reconnaissance and intelligence collection [22]. The mass of the design was estimated as a percentage of the Hermes 900's mass. The mass was refined at a

later stage in the concept's development to achieve and optimise mission performance. The final mass estimation of the design was shown in Table 4.

Table 3 Mass estimation data for the design

Parameter	Mass [kg]
MTOW	3 669.41
Payload	3
Fuel	2 916.41
Empty weight	750

There was no explicit duration for the mission. However, given the time-sensitive nature of the problem a design that completed the mission sooner rather than later was desired. The primary goal during the initial 72 hours of search and rescue was to conduct search and rescue operations to locate and assist survivors who may be trapped under debris or were in dangerous situations. The quicker these operations begin, the higher the chance of locating survivors who may be able to withstand the conditions for a limited period [23]. As a result, a mission duration of 24 hours was assumed since the design was utilised for identification of trapped victims. As the search pattern was conducted, regions that have been covered could begin with the extraction process simultaneously.

Using the mission range of 5 367.51 nautical miles and the duration of 24 hours, an average velocity target of 115.05 metres per second was determined for the design.

Several wing aspect ratio configurations were considered for the design. Drag polars were plotted, shown in Figure 23, for each wing aspect ratio while maintaining a constant C_{D_0} value of 0.02. The value of 0.02 was chosen as it assumed a relatively clean and aerodynamically efficient design, which was a reasonable starting point for preliminary design calculations.

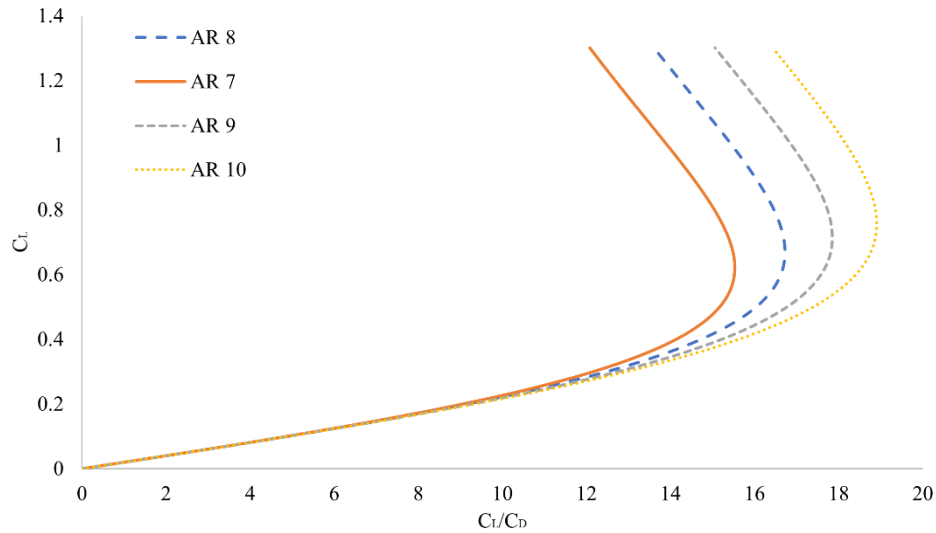


Figure 23 Effect of the design's wing aspect ratio on maximum lift-to-drag ratio

From Figure 23, it was evident that a higher wing aspect resulted in a larger maximum lift-to-drag ratio. However, the larger maximum lift-to-drag ratio corresponded to a higher lift coefficient. Hence, for a higher wing aspect ratio the concept needed to be designed to travel at a lower velocity due to the higher lift coefficient. This was needed to maintain the maximum lift-to-drag ratio. The corresponding numerical values for this was shown in Table 5.

Table 4 Effect of the design's wing aspect ratio on maximum lift-to-drag ratio

Wing aspect ratio	Maximum lift-to-drag ratio	Lift coefficient at maximum lift-to-drag ratio
7	15.52	0.6
8	16.72	0.65
9	17.84	0.7
10	18.90	0.75

A wing aspect ratio of 8 was chosen for the design as it permitted a high lift-to-drag ratio at a relatively low expense of the corresponding lift coefficient.

Various airfoils were explored for the wing of the design. The zero-lift pitching moment coefficient and maximum lift coefficient were used as criteria to select an airfoil. The zero-lift pitching moment coefficient was used as a criterion to ensure that there was minimal pitching moment due to the wing. This was desirable as the mission profile primarily consisted of the cruise phase. Excessive pitching moment caused by the wing while cruising would require a larger tail to ensure a moment equilibrium. The maximum lift coefficient was used as a criterion to ensure a low stall speed for the design. A low

stall speed was desirable as it allowed take-off and landing at lower speeds. This directly correlated to a shorter length of runway required. Lower stall speeds permitted the design to generate sufficient lift at lower speeds, allowing for more fuel to be carried while still maintaining safe take-off and landing characteristics.

A NACA 23024 airfoil was chosen for the wing of the design. The airfoil was well-balanced in terms of the criteria used for evaluation. Other potential airfoils that were considered had a large maximum lift coefficient at the expense of a larger pitching moment or vice versa. Table 6 showed the properties for the NACA 23024 airfoil while Figure 24 depicted the airfoil profile.

Table 5 NACA 23024 airfoil properties [27]

Airfoil property	Value
α_0	-0.8°
C_{M_0}	0
C_{L_α}	0.097 per degree
Aerodynamic centre	23.1% MAC
$C_{L_{max}}$	1.40

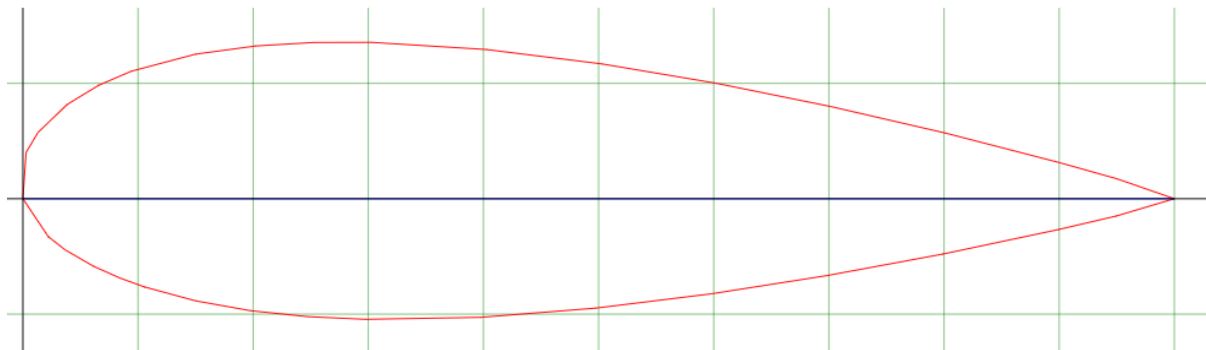


Figure 24 NACA 23024 airfoil profile [28]

The altitude for the mission was 5 085.3 ft above the surface of the disaster-stricken region. The altitude above sea level was determined by adding the altitude of the search terrain. The altitude above sea level for the mission was 5 816.93 ft. This corresponded to a density ratio of 0.8406. A stall velocity of 90 metres per second was assumed since the average velocity of the design was 115 metres per second to perform the mission within 24 hours. This provided enough safety margin as there was a buffer of 25 metres per second between the stall speed and cruise velocity of the design.

Using the MTOW of 3 669.41 kg, the wing area was calculated for the design using:

$$C_{L_{max}} = \frac{2 * M * g}{\rho * \sigma * S * V_s^2}$$

(5) [29]

The wing area was 6.17 m^2 . The lift distribution of the wing was compared for various taper ratios. The lift distribution for each wing configuration was obtained using Tornado, a free MATLAB code that utilised the Vortex Lattice Method to compute lift generation. The wing geometry and flight conditions were initialised for each wing configuration in Tornado. The NACA 23024 airfoil data was obtained from Airfoil Tools [28]. A compressibility correction was not applied since the flight velocity was relatively low. Table 7 contained the flight conditions that were kept constant for the computations. All wing configurations were discretised into ten semi-span panels and five chord-wise panels, as shown in Figure 25. The discretisations were kept constant for all computations to ensure a fair comparison.

Table 6 Tornado input parameters used to obtain lift distribution

Flight condition parameter	Value
Angle of attack	0°
True airspeed	$113.23 \frac{\text{m}}{\text{s}}$
Altitude	5 816.93 ft

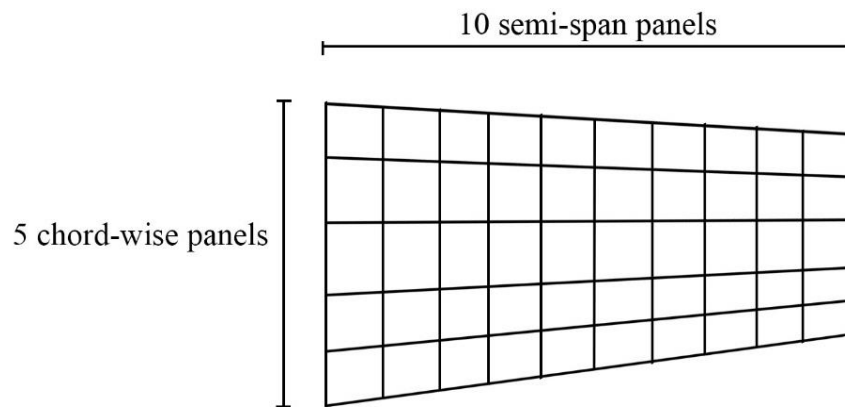


Figure 25 Discretisations for each wing configuration

The lift distribution data for all wing configurations was exported to Microsoft Excel 2016 to produce Figure 26, which showed the effect of wing taper ratio on the lift distribution of the wing.

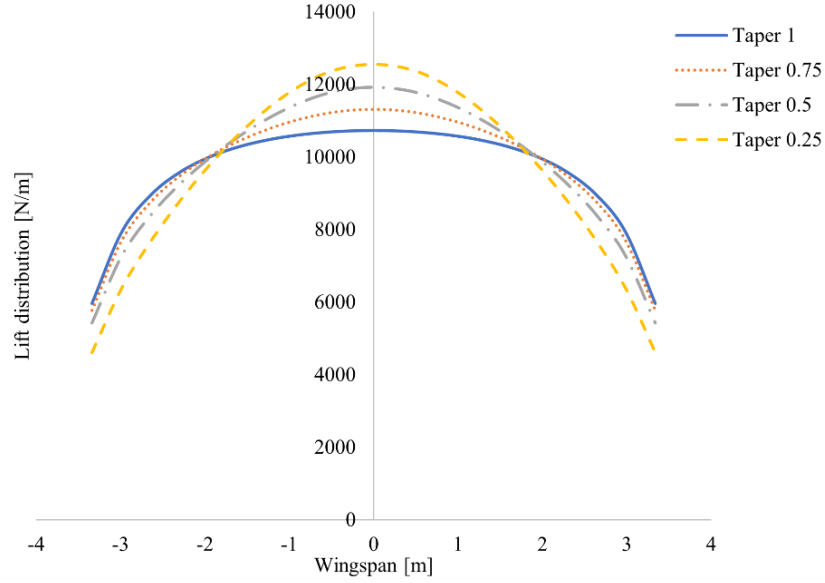


Figure 26 Effect of wing taper ratio on lift distribution

Figure 26 showed that a larger taper ratio resulted in more lift generation at the wing tips compared to lower taper ratios. However, this came at the expense of reduced lift generation at the wing root. Furthermore, a larger taper ratio tended to cause a relatively constant lift distribution near the wing root. For lower taper ratios, the peak lift generated at the wing root became more distinct with a more drastic decrease in lift toward the wing tips. Additionally, lower taper ratios resulted in a lower mass for the wing since there was effectively less material used for the wing. A taper ratio of 0.75 was selected for the design as it was the closest resemblance to an elliptical lift distribution. This meant that there was a reduction in lift-induced drag and a more gradual stall behaviour.

The feasibility of a manned versus unmanned design was considered. Unmanned aircraft could be deployed and operated round the clock without the limitations of human crew rest requirements. This ensured continuous coverage, especially during critical early response phases when time is critical. Autonomous designs can maintain consistent flight parameters, which is particularly important for tasks like data collection. This consistency ensures high-quality data and reduces human error. Hence, an autonomous design was opted for.

The pitching moment coefficient for the wing about the centre of gravity position was considered using:

$$C_{M_{CG}} = C_{M_0} + C_L(h - h_0) \quad (6)$$

Since the design was autonomous, $h = h_0$. Hence, the pitching moment coefficient for the wing was always zero since C_{M_0} for the airfoil was zero from Table 6. This indicated neutral stability of the wing

at all speeds. The wing did not induce a nose up or down pitching moment. Table 7 showed the final wing geometry while Figure 27 showed the 3D model of the finalised wing.

Table 7 Wing geometry for the design

Geometric parameter	Value
Aspect ratio	8
Span	7.02 m
Reference area	6.17 m^2
Root chord	1 m
Tip chord	0.75 m
Mean aerodynamic chord	0.88 m
$Sweep_{\frac{1}{4} \text{ chord}}$	4.09°
Taper ratio	0.75

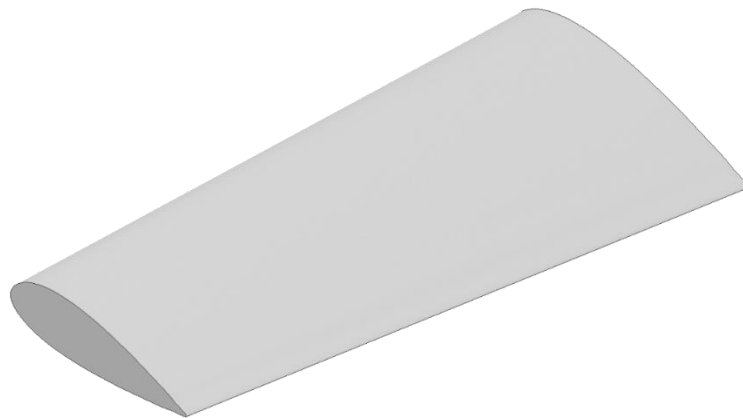


Figure 27 3D model of the wing

Once the wing was designed, focus was shifted onto the sizing of the empennage. For the horizontal and vertical tail, a NACA 0009 airfoil was utilised. The airfoil was chosen due to being symmetrical and having no zero-lift pitching moment. The symmetry was advantageous as the tail setting would not need to be positioned at an angle of attack relative to the wing in order to maintain pitch stability.

The horizontal tail arm was found using:

$$L_{HT} = \frac{V_{HT} * S * MAC}{S_{HT}}$$

(7) [30]

The inputs for equation (7) are available in Appendix A. The horizontal tail arm was calculated to be 1.98 m. The aspect ratio for the horizontal tail was set to 4, which was half the aspect ratio of the wing.

The sweep for the horizontal tail was set to 5° more than the wing sweep. This was done to ensure that the wing stalled first and prevented loss of elevator control at stall. In the event of a stall, there would still be control of the elevator and this increased the likelihood of recovering from the stall. Table 8 showed the final horizontal tail geometry while Figure 28 showed the 3D model of half of the horizontal tail.

Table 8 Horizontal tail geometry for the design

Geometric parameter	Value
Aspect ratio	4
Span	2.72 m
Reference area	1.85 m ²
Root chord	0.94 m
Tip chord	0.42 m
Mean aerodynamic chord	0.71 m
$Sweep_{\frac{1}{4}chord}$	9.09°
Taper ratio	0.45
Horizontal tail arm	1.98 m

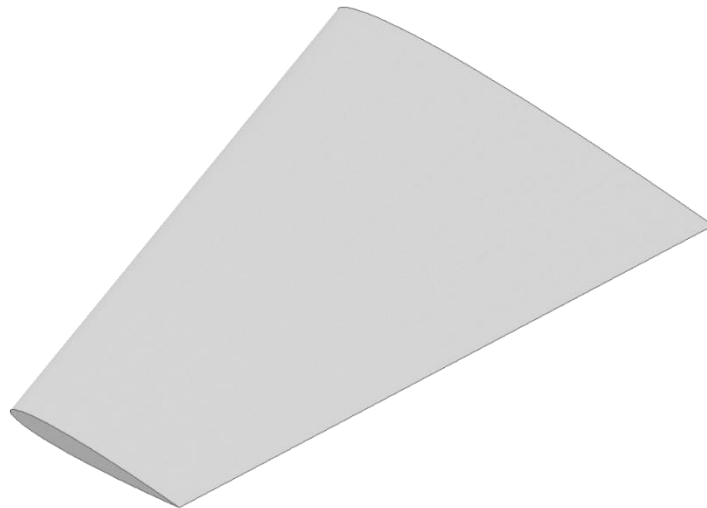


Figure 28 3D model of the horizontal tail

A similar approach was applied when designing the vertical tail. The vertical tail reference area was found using:

$$S_{VT} = \frac{b * V_{VT} * S}{L_{VT}}$$

(8) [30]

The inputs used for equation (8) are available in Appendix A. The vertical tail reference area was determined as 1.38 m^2 . The final vertical tail geometry was shown in Table 9. The sweep angle of the vertical tail was increased by 6 degrees more than that of the horizontal tail. This was done to improve yaw damping which helped to suppress unwanted yawing motions. Proper yaw damping was important for the design as it ensured stability under undesired conditions such as crosswinds. The aspect ratio for the vertical was much lower than that of the horizontal tail and wing. The motive behind this was that smaller vertical tails create less interference drag and potentially contribute to improved overall aerodynamic efficiency. Figure 29 illustrated the 3D model of the vertical wing.

Table 9 Vertical tail geometry for the design

Geometric parameter	Value
Aspect ratio	1.65
Span	1.51 m
Reference area	1.38 m^2
Root chord	1.26 m
Tip chord	0.57 m
Mean aerodynamic chord	0.96 m
$Sweep_{\frac{1}{4} \text{ chord}}$	15°
Taper ratio	0.45

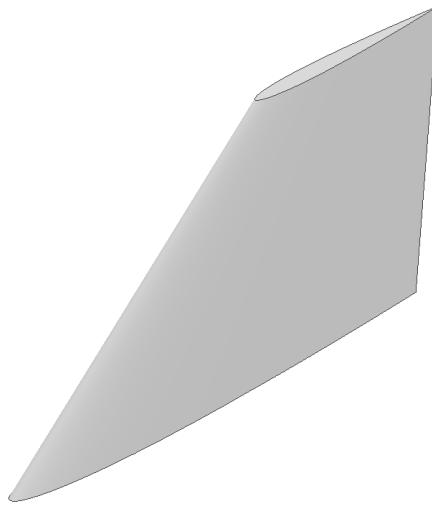


Figure 29 3D model of the vertical wing

The empennage and wing were designed. The sizing of the fuselage was then focused on. This was done in conjunction with a calculation of the parasite drag coefficient to determine the effect of fuselage sizing on the drag coefficient in an iterative manner. With initial fuselage sizing, the parasite drag coefficient was 0.02817. The fuselage was then iteratively resized to reduce the parasite drag coefficient. The drag coefficient was reduced by 12.11% to a final value of 0.02476. The fuselage profile was made up of a cylinder with ogive cones at the nose and tail of the design. The ogive-shaped nose at the front of the fuselage assisted in smoothly transitioning the incoming airflow around the fuselage. This reduced aerodynamic drag by minimizing the disruption caused by the sudden change in cross-sectional area that occurred with a flat or blunt nose. The ogive-shaped nose at the rear of the fuselage assisted in smoothly transitioning the airflow as it separated from the fuselage. This minimized the formation of turbulent wake and eddies, which led to increased drag and reduced overall aerodynamic efficiency.

The total fuselage length was 6.08 m. The bookkeeping drag table is available in Appendix B. Excrescences, which included external lights and antennas, were taken into account when calculating the parasite drag coefficient. Figure 30 showed the final fuselage shape.

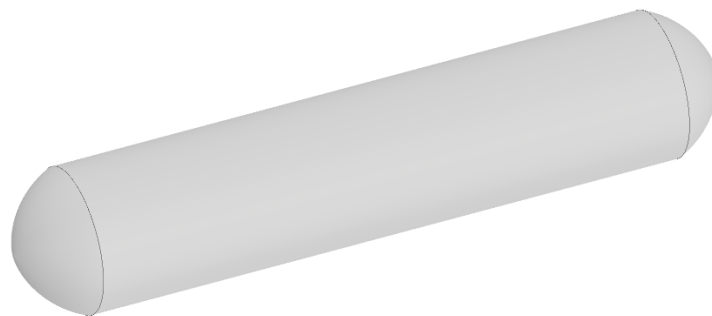


Figure 30 3D model of the fuselage

A graph of drag force was plotted over a range of velocities. This was done to establish a thrust benchmark for the propulsion system for the design. Two potential engines, the Pratt & Whitney Canada PT6-25A and Honeywell TPE331-10, were identified for the design. The specifications for both engines were shown in Table 10.

Table 10 Comparison of potential engines for the design

Performance parameter	Pratt & Whitney Canada PT6A-25A	Honeywell TPE331-10A
Maximum continuous power	550 hp [31]	900 hp [32]
Specific fuel consumption	$0.63 \frac{lb}{hp.hr}$ [33]	$0.55 \frac{lb}{hp.hr}$ [33]
Mass	160 kg [31]	174.63 kg [32]

The Honeywell engine was a better choice in terms of maximum continuous power and specific fuel consumption. However, it was at the expense of a larger mass. Thrust curves for both engines were generated and superimposed onto the graph of drag force. This was done to illustrate the differences in engine performance and establish whether the increased mass of the Honeywell engine was worth the additional power gain. Figure 31 compared the thrust for both engines with the drag for the design. The calculations used to obtain the thrust data for Figure 31 is available in Appendix A.

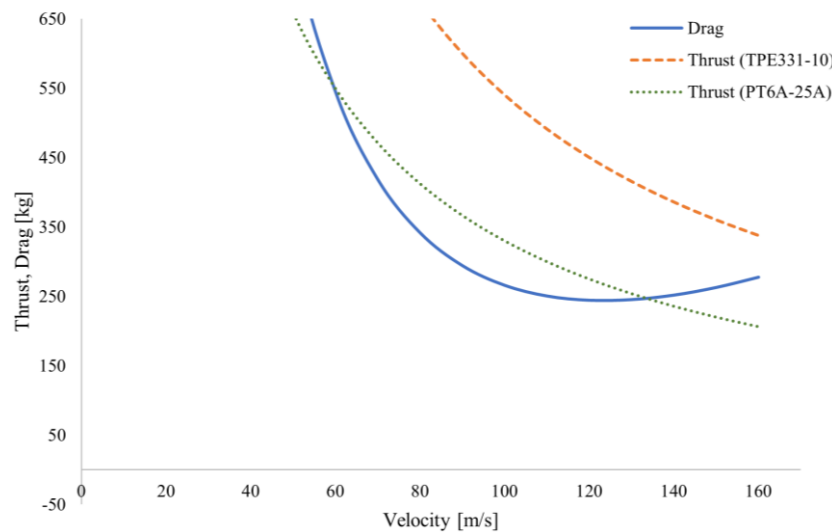


Figure 31 Thrust comparison of engines at cruise altitude

From Figure 31, it was seen that the TPE331-10 engine performed better than the PT6A-25A engine. This was evident over all velocities at the cruise altitude. The PT6A-25A engine was only able to produce more thrust than drag over the velocity range from $60 \frac{m}{s}$ to $140 \frac{m}{s}$. This posed an issue if the design travelled at velocities greater than $140 \frac{m}{s}$. It was unlikely that the design travelled below $60 \frac{m}{s}$ because the stall speed was $90 \frac{m}{s}$. The Honeywell TPE331-10 engine was selected for the design as it

produced more thrust than drag over all velocities. Additionally, the engine had a lower fuel consumption which permitted more range as the fuel consumption was lower.

The minimum drag point, obtained from Figure 31, was at a velocity of $126 \frac{m}{s}$. At this point the design experienced 233.53 kg of drag force while the selected Honeywell engine was capable of producing 428.57 kg of thrust. Since the design was cruising while performing the search pattern, the actual thrust output was 240.75 kg as this took into account 3% engine losses. The engine losses included friction losses between moving parts in the engine as well as combustion losses like unburned fuel in the exhaust. [34]

The diameter for the fuselage cross-section was 1.22 metres. The selected engine had a maximum diameter of 0.68 metres and length of 1.09 metres. Hence, the engine was able to fit within the fuselage while the rotating propeller protruded. The engine was positioned at the rear of the design in a pusher configuration. This was done to ensure additional space in the nose area of the design, allowing for easier integration of the camera modules that detected the trapped victims. Placing the propeller at the rear of the design minimized the impact of engine vibrations and noise on the camera sensors placed at the front of the design. This was important for maintaining high-quality data acquisition and transmission to ground rescue personnel. Figure 32 showed the configuration of the turboprop engine and propeller integrated into the fuselage.

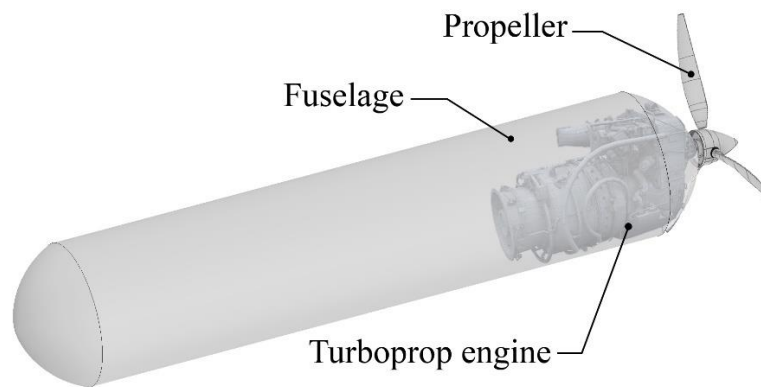


Figure 32 3D model of translucent fuselage with integrated turboprop engine and propeller

With the fitment of the engine integrated into the fuselage, the partition for fuel was determined. The engine occupied 1.09 metres in length from the rear. A length of 1 metre from the front of the fuselage was reserved for storage of electronic modules. Hence, a remainder length of 3.99 metres was kept for fuel storage. This computed to a volume of $4.63 m^3$. From the mass estimation data in Table 3, the fuel mass was 2 916.41 kg. The density of Avgas (Aviation gasoline) was $0.7959 \frac{g}{ml}$ [35]. Based on the mass estimation data and density of Avgas, the design required a volume of $3.66 m^3$ for fuel. Hence, the

volume of 4.63 m^3 for fuel storage was sufficient for the mission. To minimise the effects of fuel sloshing in the design, the fuel tank was resized to ensure that the volume exactly equated to 3.66 m^3 . This change permitted more space for storage of electronics and modules. Baffles were not needed to be designed as the fuel tank was always filled to the maximum level, resulting in minimal fuel sloshing. Figure 33 showed a cross-section of the fuselage depicting the use for each segment.

*Illustration not to scale

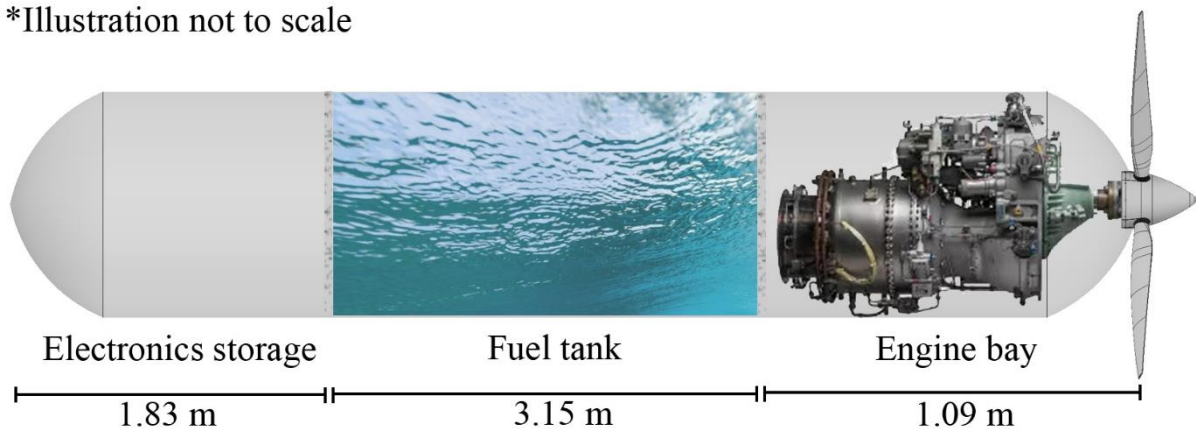


Figure 33 Cross-section of the fuselage

The search pattern consisted of parallel search legs joined by alternating manoeuvre points, as shown in Figure 34.

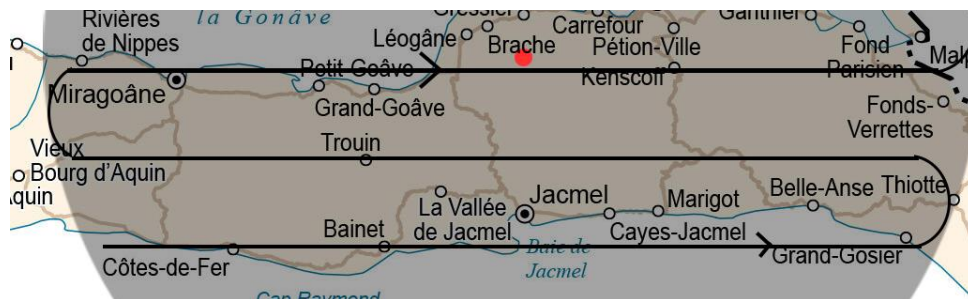


Figure 34 Parallel search legs joined by manoeuvre points [21]

The design was required to turn at the manoeuvre points in order to re-position to begin the subsequent search leg. Since the search legs were parallel, the turn manoeuvre was effectively the same between all search legs. The turn performance of the design was calculated. The design was required to perform a level turn as there was no altitude gain between adjacent search legs.

The level turn equation used for the computation was:

$$R = \frac{V^2}{g\sqrt{n^2 - 1}}$$

(9) [36]

The inputs for equation (9) are available in Appendix A. The turn velocity required to perform the level turn between each search leg was $107.362 \frac{m}{s}$. This was advantageous as it was above the design stall speed of $90 \frac{m}{s}$.

The turn rate for the manoeuvre was found using:

$$\omega = \frac{g * \sqrt{n^2 - 1} * 180}{V * \pi}$$

(10) [36]

The inputs used for equation (10) were the same as those used for equation (9). The turn rate for the manoeuvre was $12 \frac{^\circ}{s}$. An interpretation for this was shown in Figure 35.

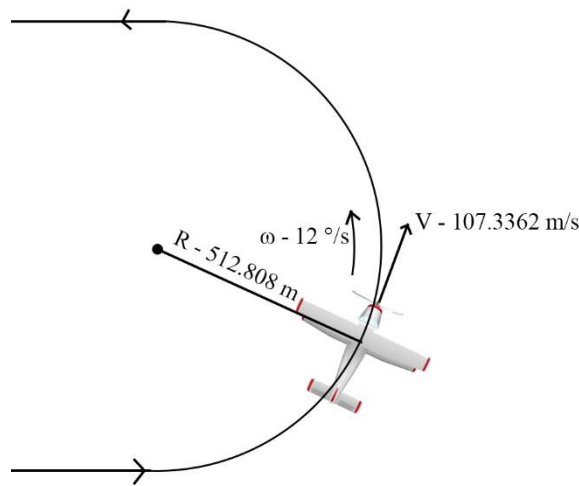


Figure 35 Interpretation for the turn manoeuvre performed by the design

The design had a stall speed of $90 \frac{m}{s}$. This meant that it needed a conventional runway to take-off and land since the stall speed was within the range of many conventional aircraft. The field performance for the design was calculated for take-off at Antoine-Simon Airport as it was the closest airport outside the affected region. This ensured swift deployment for the design due to the time-sensitive nature of the problem. Landing field performance was calculated at Hinche Airport. This was the closest airport to the end of the search pattern outside the affected region. Figure 36 showed the locations of both airports in relation to the affected region.

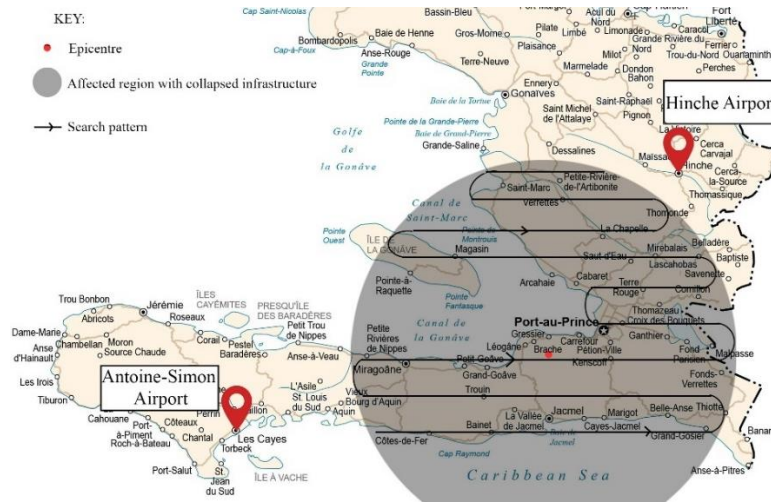


Figure 36 Location of take-off and landing airports utilised by the design

Antoine-Simon Airport only had one runway with a length of 981 metres [37]. The runway length at Hinche Airport was 861 metres [38]. Figure 37 showed the field performance calculated for the design. The runway lengths were included as a reference.

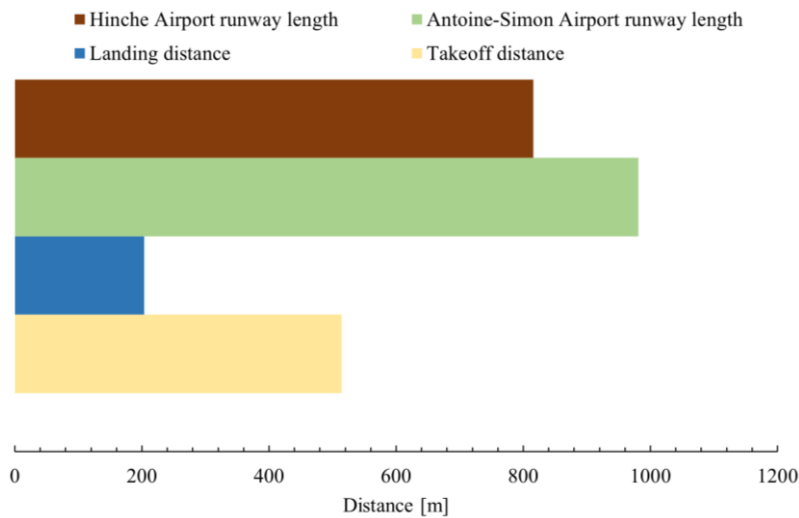


Figure 37 Field performance for the design

The design utilised approximately 52% of the available runway to take-off. For landing, 25% of available runway was used. Hence, Antoine-Simon Airport and Hinche Airport were ideal for the design to utilise.

The design was evaluated by assessing the performance parameters and determining whether it was sufficient for the mission. Based on the cruise velocity and specific fuel consumption, the duration for all fuel to burn was calculated along with the corresponding range. The duration was 21.05 hours while the range was 5 421.12 nautical miles. This was adequate as the mission required a range of 5 367.51

nautical miles. After completing the mission, there was remaining fuel that permitted 53.61 nautical miles of flight.

6. Design integration

The designed aircraft was essentially based on specifications from the combination of thermal cameras. The altitude, number of search legs required and the need for an aircraft was established from the thermal cameras' specifications. It was therefore imperative that both designs were integrated to ensure an efficient and functional solution.

The camera system consisted of one camera positioned vertically downward while the remaining two cameras were positioned at 27.2 degrees relative to the single camera in opposite directions. The camera modules did not consist of a mechanism that allowed it to be mounted onto the aircraft. The cameras did not have the ability to pan or tilt. However, this was not required as the aircraft traversed while the camera modules remained fixed onto the aircraft.

A mount was designed that allowed the camera modules to be attached to the aircraft. The mechanism was placed under the fuselage near the front of the aircraft. This was done to ensure there were no distractions in the captured image as the propeller was moved to the rear of the aircraft. Several camera configurations were explored before the mount was designed.

The outer cameras in Figure 38 were rotated at 27.2° relative to the centre camera. They were positioned adjacent to each other. This was done to ensure that all thermal cameras capture maximum ground coverage without duplication of images.

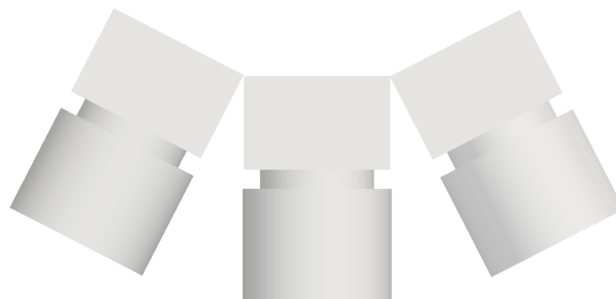


Figure 38 Adjacent arrangement of thermal cameras

The layout in Figure 39 combined the thermal cameras in a triangular arrangement. The cameras at the top were rotated at 27.2° while the bottom camera was positioned vertically downward.

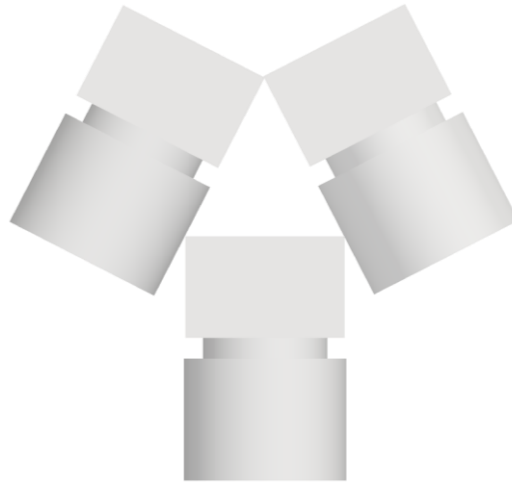


Figure 39 Triangular arrangement of thermal cameras

The layout in Figure 40 consisted of thermal cameras joined adjacent to one another. There was a possibility of overlapped images due to the outer cameras only being rotated horizontally. This meant that there was effectively a blind spot in the vertical axis of the image as well as the likelihood of duplicated regions in the horizontal axis of the image, making it a non-ideal configuration.

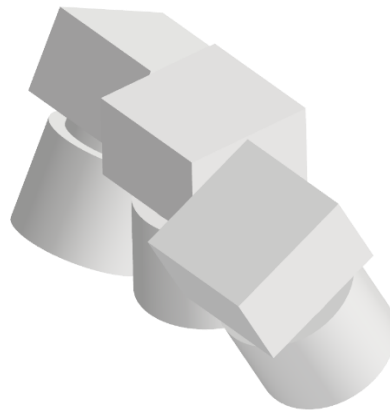


Figure 40 Conjoined arrangement of thermal cameras

The adjacent arrangement in Figure 38 was selected as the ideal layout for the thermal cameras. The arrangement provided optimal ground coverage without duplication of images. The triangular arrangement was irregular as the mount would have had limited clearance to provide enough stability for the lower camera. This was identified as a potential issue and the adjacent arrangement was therefore utilised. Figure 41 showed the dimensions for the selected camera configuration.

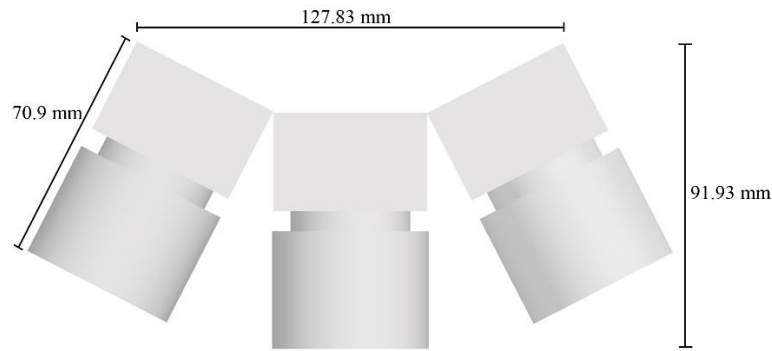


Figure 41 Camera configuration with annotated dimensions

The mount was designed to hold all thermal cameras in a fixed position that did not permit tilting or panning of the cameras. This was done to ensure that there was no possibility of blind spots and duplicated regions in the captured images. If the cameras were positioned closer to one another then it would result in an overlap of field of views, producing images with duplicated regions. Conversely, if the cameras were positioned further apart then it would result in unscanned regions located between the captured regions. Figure 42 showed an annotated view of the designed mount.

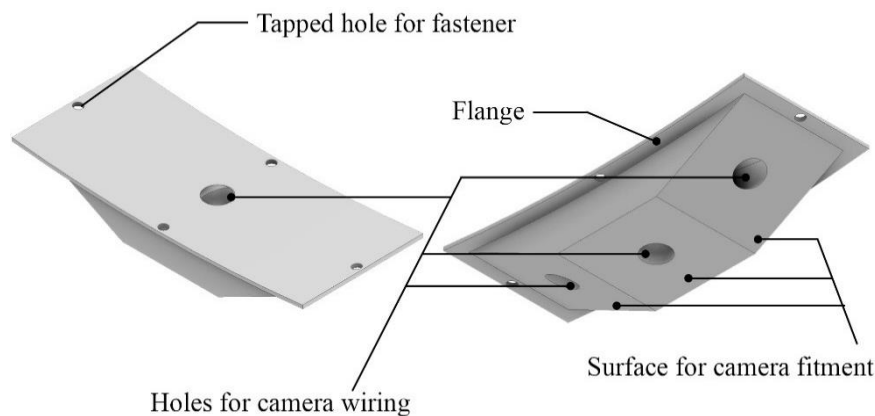


Figure 42 Annotated 3D view of the designed mount

The top of the mount was curved to ensure flush fitment onto the curved fuselage. The bottom of the mount was segmented into three surfaces to allow the rear of the thermal cameras to fit onto the mount. The mount was designed to be as small as possible but still functional. A small mount was ideal to ensure minimal disturbances of airflow below the fuselage. The form factor was kept to a minimum by accounting for direct fitment of the cameras onto the mount. The mount was designed to be attached to the fuselage by means of a flange. The flange allowed the secure attachment of the mount and addition of fasteners which ensured rigidity of the cameras. The flange was provided with enough clearance such that the fasteners did not protrude into the region where the cameras fit. The fasteners used to fit the mount onto the fuselage was DIN 920 M4x4. They were fastened through four tapped holes in the mount. Lofted holes were included for all three cameras to allow routing of the camera wiring. The

holes at the bottom of the mount led to a single hole at the top of the mount. Since the attachment of the mount was flush onto the fuselage, a hole below the fuselage of the same diameter as that on top of the mount was created to route all camera wiring. This ensured safe routing of wiring as well as a minimal number of holes to maintain structural rigidity of the mount. A schematic of how the cameras fit onto the mount was shown in Figure 43.

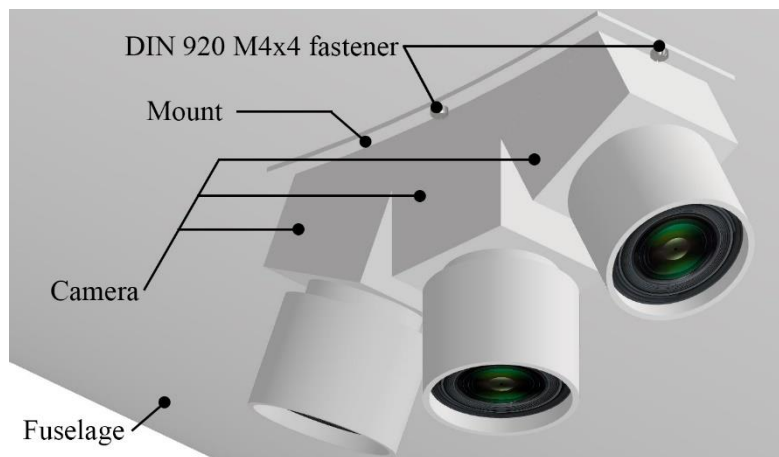


Figure 43 Schematic of integration of cameras, mount and fuselage

7. Design specifications

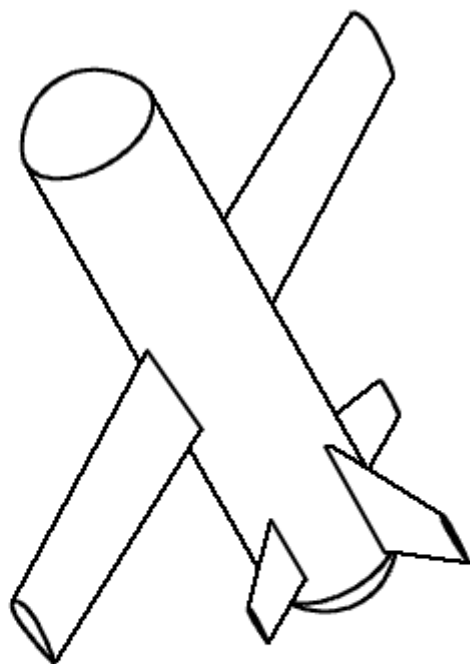
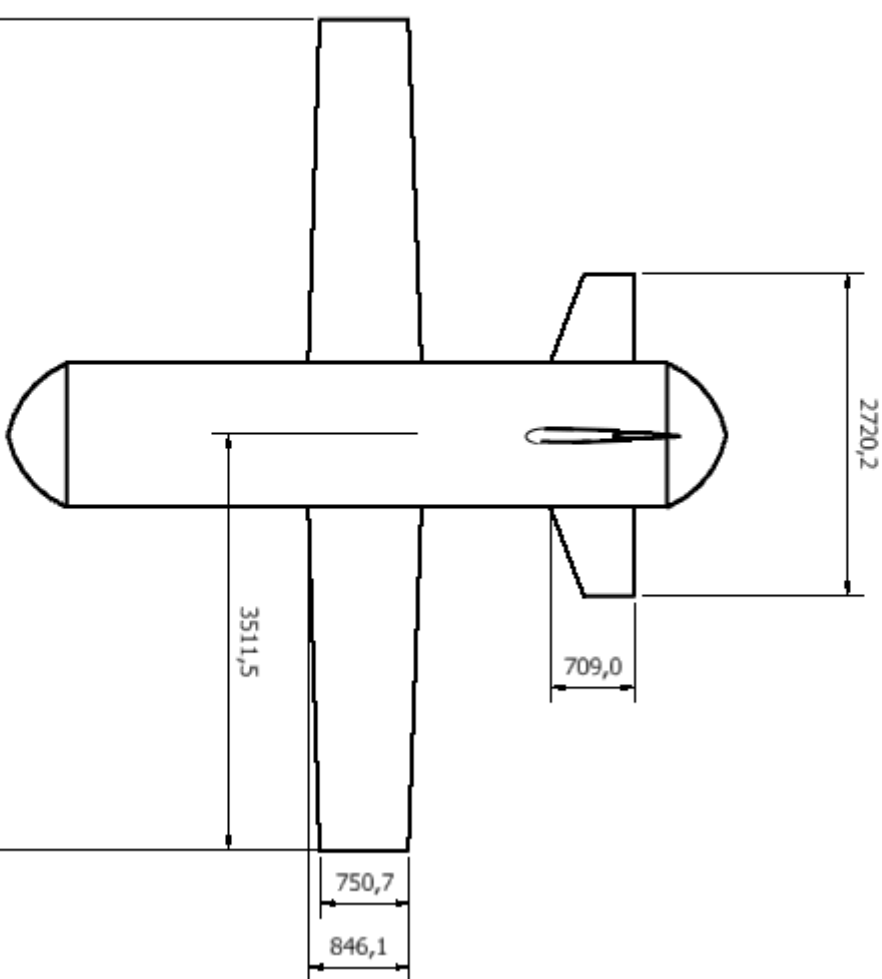
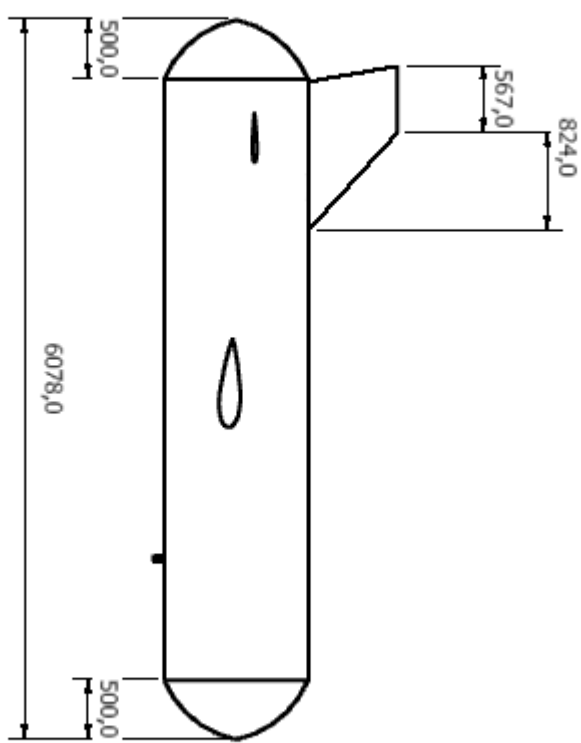
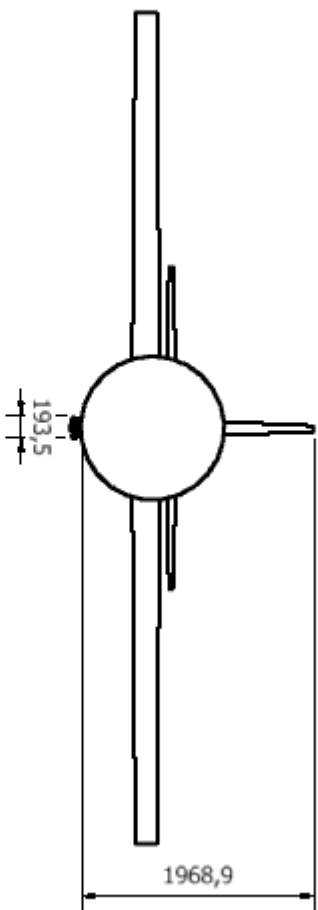
The designed aircraft was an unmanned aerial vehicle with a conventional tail design. The primary source of lift was a tapered, rearward-swept wing. The design was powered by a turboprop engine capable of outputting 671 kilowatts. The turboprop engine was constructed in a pusher configuration positioned at the rear of the fuselage. Three thermal cameras were attached to the fuselage by means of a designed mount. The mount was secured to the fuselage by four slotted pan head screws. The integration of the cameras and aircraft permitted the cameras to capture a total ground surface area of 0.2805 km^2 in a single image. In addition to this, the design was able to detect trapped victims at a maximum of five metres below surface rubble. Table 11 contained the performance specifications for the integrated design.

Table 11 Summary of performance specifications for integrated design

Parameter	Value
Focal length	100
Frame rate	30 Hz
Ground covered in a single image	0.2805 km^2
Fuel capacity	2 916 kg
MTOW	3 669 kg
Range	5 421 nmi
Cruise velocity	$126 \frac{\text{m}}{\text{s}}$
Stall speed	$90 \frac{\text{m}}{\text{s}}$
C_{D_0}	0.02476
Endurance	21 hours
Take-off distance (over a 35 ft obstacle)	531 metres
Landing distance (over a 35 ft obstacle)	204 metres

The aircraft and mount were designed to be manufactured using 7075 aluminium. The material was well-suited because of its excellent balance between strength and weight, outstanding resistance to corrosion, and favourable fatigue resistance [39]. Due to the mission profile consisting of parallel search legs and manoeuvre points, the good fatigue resistance capabilities endured repeated cyclic loads on critical components such as the wing and camera mount. It was vital that the mount was manufactured using a high strength-to-weight material, such as 7075 aluminium, because of its critical role in ensuring integration of the thermal cameras and aircraft. Without integration, the design was not a functional solution.

The engineering drawings for the final integrated design was shown on the next page. The engineering drawings for each part making up the integrated design are available in Appendix C.



APPROVED:	
DATE: 04/09/2023	
DRAWN BY: Castello	
NOTES: SURFACE FINISH ∇ UNLESS OTHERWISE STATED. DIMENSIONS IN mm. DO NOT SCALE. ALL THREADS MEDIUM FIT. ASSEMBLY:	
SCALE: 1:45	
QTY:	
DRG NO:	REV NO.
DESCRIPTION: Integrated design	
MATERIAL:	



SCHOOL OF MECHANICAL, INDUSTRIAL AND AERONAUTICAL ENGINEERING,
UNIVERSITY OF THE WITWATERSRAND,
JOHANNESBURG.



8. Critical assessment of design

The integrated design was capable of completing the mission profile. Operating with a full tank of fuel, the design was able to achieve a range of 5 421 nautical miles. This was sufficient for the mission which required a range of 5 368 nautical miles. The remaining range of 53 nautical miles was adequate for loitering before landing due to unexpected delays at the airport. The initial assumption for the mission duration of 24 hours was largely dependent on the likelihood of survival within the 72 golden hours in search and rescue operations. The design had good performance as it was able to complete the mission in 21 hours. Furthermore, the design had adequate field performance as it utilised 52% of available runway for take-off and 25% for landing.

The requirements in §4 were met by use of the thermal cameras and aircraft. The thermal cameras permitted the design to detect and identify trapped victims five metres below the surface of rubble. The aircraft was developed to ensure that the cameras scan the entire disaster-stricken region. This was achieved through flight over the region in a creeping line search pattern. The integrated design was able to operate under all weather conditions experienced in Haiti. Adverse weather conditions were not an issue as the aircraft was an UAV with a turboprop engine.

The constraints in §4 were met by the development of the aircraft. Since the solution traversed the region aurally, the stability of the rubble did not need to be investigated as the thermal detection was a non-contact method. The thermal camera was selected based on various parameters to overcome the constraint of image resolution. The operating distance of the camera was directly affected by the resolution of the camera. This was accounted for when selecting an ideal camera for the solution. The optimal operating distance of the camera was achieved by use of the designed aircraft.

Each sub-component of the design was designed and optimised individually. After all computations and individual designs were done, the integrated design was optimised by iterating the mass and fuselage sizing to ensure a maximum range and minimised mission completion time according to the criteria in §4. This resulted in an optimal, functional solution.

8.1 Operating cost

The designed aircraft required Avgas to operate. At the time of writing, the price of Avgas was \$0.562 (R10.74) per litre in Haiti [40]. Using the 3 660-litre fuel capacity of the design, the cost to fill the fuel tank was \$2 056.92 (R39 325). This operating cost of R39 325 was to ensure that the mission was completed in terms of range to cover the disaster-stricken region once. If multiple scans of the same region were required, then the fuel tank needed to be filled again to maximum capacity, costing R39 325, to fulfil the same mission.

8.2 Recommendations for further work

The implementation of artificial intelligence algorithms, such as object recognition and anomaly detection, can be done to automate the process of identifying potential victims in the captured thermal imagery, reducing remote operator workload and potentially improving accuracy. All calculations done in this design report was theoretical. A prototype design can be manufactured and flight tests conducted to obtain real-world performance specifications for the design. Rigorous field testing and validation exercises can be conducted in simulated disaster scenarios to evaluate the design's performance, reliability, and effectiveness under real-world conditions. This will likely differ from the theoretical calculations made. Improvements of the design can be conducted once the flight test data is obtained and analysed. Modifications of the design can be explored to permit ease of adaptability to other geographical regions that are susceptible to earthquakes.

9. References

- [1] Earthquake Hazards Program, “National Earthquake Information Center (NEIC),” U.S. Geological Survey. <https://www.usgs.gov/programs/earthquake-hazards/national-earthquake-information-center-neic> (accessed Jul. 20, 2023).
- [2] United States Geological Survey, “At what magnitude does damage begin to occur in an earthquake?,” U.S. Geological Survey. <https://www.usgs.gov/faqs/what-magnitude-does-damage-begin-occur-earthquake> (accessed Jul. 20, 2023).
- [3] Statista, “Number of earthquakes globally 2000-2021,” Statista, Aug. 05, 2022. <https://www.statista.com/statistics/263105/development-of-the-number-of-earthquakes-worldwide-since-2000/> (accessed Jul. 20, 2023).
- [4] M. Armstrong, “Infographic: The World’s Deadliest Earthquakes,” Statista, Jan. 09, 2020. <https://www.statista.com/chart/20443/deadliest-earthquakes-since-1900/> (accessed Jul. 20, 2023).
- [5] D. Sweeney and S. Ortiz-Blanes, “Why does Haiti have so many earthquakes? Here’s what to know,” Miami Herald, Aug. 14, 2021. <https://www.miamiherald.com/news/nation-world/national/article253492439.html> (accessed Jul. 20, 2023).
- [6] WorldData, “Recent earthquakes and their magnitudes in Haiti,” Worlddata.info. <https://www.worlddata.info/america/haiti/earthquakes.php> (accessed Jul. 20, 2023).
- [7] Jitesh Chowdhury, S. Scarr, and A. Arranz, “How search and rescue teams pull survivors from rubble,” Reuters, Feb. 09, 2023. Accessed: Jul. 21, 2023. [Online]. Available: <https://www.reuters.com/graphics/TURKEY-QUAKE/SEARCH/klpygdjoapg/>
- [8] D. S. with Agencies, “Chances of survival may be up to a week after earthquakes: Experts,” Daily Sabah, Feb. 09, 2023. Accessed: Jul. 21, 2023. [Online]. Available: <https://www.dailysabah.com/turkey/chances-of-survival-may-be-up-to-a-week-after-earthquakes-experts/news>
- [9] Hikers Bay, “Data tables and charts monthly and yearly climate conditions in Haiti,,” hikersbay, Mar. 19, 2018. <http://hikersbay.com/climate-conditions/haiti/climate-conditions-in-haiti.html?lang=en#weather-temperature-months> (accessed Jul. 25, 2023).
- [10] TripReport, “Climate and Weather in Haiti,” Trip Report. <https://www.tripreport.com/countries/haiti/climate> (accessed Jul. 25, 2023).
- [11] R. Pallardy, “2010 Haiti earthquake,” Encyclopaedia Britannica, Jan. 15, 2010. Accessed: Aug. 14, 2023. [Online]. Available: <https://www.britannica.com/science/natural-disaster>

- [12] R. Valls, "The Geology and Mineral Resources of Northern Haïti.," Apr. 30, 2019. https://www.researchgate.net/publication/332776671_The_Geology_and_Mineral_Resources_of_Northern_Haiti (accessed Aug. 14, 2023).
- [13] Teledyne FLIR, "Lepton LWIR Micro Thermal Camera Module," Teledyne FLIR. <https://www.flir.eu/products/lepton/?model=500-0771-01&vertical=microcam&segment=oem> (accessed Aug. 02, 2023).
- [14] mixos, "FLIR Lepton 3.0 & 3.5 Micro Thermal Camera Modules," Electronics-Lab.com, Apr. 27, 2021. <https://www.electronics-lab.com/flir-lepton-3-0-3-5-micro-thermal-camera-modules/> (accessed Aug. 02, 2023).
- [15] Infrared Cameras, "IR Inspector," Infrared Cameras. <https://infraredcameras.com/products/ir-inspector> (accessed Aug. 02, 2023).
- [16] "SWIR 640 P-Series," Infrared Cameras Inc. <https://infraredcameras.com/products/swir-640-p-series> (accessed Aug. 15, 2023).
- [17] Leonardo DRS and Electro-Optical & Infrared Systems, "How to Assess Thermal Camera Range Capability for Site Design Purposes." Accessed: Aug. 04, 2023. [Online]. Available: https://www.leonardodrs.com/media/10494/201705_truth_about_rangedata_mr-2014-10-683_rev02.pdf
- [18] Australian Museum, "Decomposition - Body Changes," The Australian Museum, Oct. 22, 2020. <https://australian.museum/about/history/exhibitions/death-the-last-taboo/decomposition-body-changes/> (accessed Aug. 08, 2023).
- [19] NCSU GeoForAll Lab, "Flight Planning (Lecture 4) - part 2," YouTube. Jan. 30, 2018. Accessed: Aug. 07, 2023. [Video]. Available: <https://www.youtube.com/watch?app=desktop&v=BjPzNXGkJOY>
- [20] World Data, "Haiti: country data and statistics," Worlddata.info. <https://www.worlddata.info/america/haiti/index.php> (accessed Aug. 10, 2023).
- [21] GISGeography, "Map of Haiti," GIS Geography, Jul. 06, 2021. <https://gisgeography.com/haiti-map/> (accessed Aug. 16, 2023).
- [22] Elbit Systems, "HermesTM 900 - Multi-role, Medium Altitude Long Endurance (MALE)," Elbit Systems, Apr. 19, 2016. <https://elbitsystems.com/uas-hermes-900-multi-role-medium-altitude-long-endurance-male/> (accessed Aug. 19, 2023).
- [26] A. Kumar, Y. Abu Nahleh, A. Hakami, and S. J. Shim, "Application of soft systems methodology in solving disaster emergency logistics problems," ResearchGate, Jan. 01, 2014.

https://www.researchgate.net/publication/259674878_application-of-soft-systems-methodology-in-solving-disaster-emergency-logistics-problems (accessed Aug. 20, 2023).

[27] School of Mechanical, Industrial and Aeronautical Engineering, “MECN 3005 Aircraft Design 1,” University of the Witwatersrand, Johannesburg.

[28] Airfoil Tools, “NACA 23024 (naca23024-il),” Airfoil Tools. <http://airfoiltools.com/airfoil/details?airfoil=naca23024-il> (accessed Aug. 20, 2023).

[29] “Accelerated Stall Speed,” Academic Flight, Apr. 17, 2020. <https://academicflight.com/articles/accelerated-stall-speed/> (accessed Aug. 20, 2023).

[30] D. Scholz, “Empennage sizing with the tail volume complemented with a method for dorsal fin layout,” Incas Bulletin, vol. 13, no. 3, pp. 149–164, Sep. 2021, doi: 10.13111/2066-8201.2021.13.3.13.

[31] Aircraft database, “Pratt & Whitney Canada PT6A-25A,” Aircraft database. <https://aircraft-database.com/database/engine-models/pt6a-25a> (accessed Aug. 22, 2023).

[32] Honeywell Aerospace, “TPE331-10 Turboprop Engine,” 2016. Accessed: Aug. 22, 2023. [Online]. Available:

<https://aerospace.honeywell.com/content/dam/aerobt/en/documents/learn/products/engines/brochures/N61-1491-000-000-TPE331-10TurbopropEngine-bro.pdf>

[33] N. Meier, “Civil Turboshift/Turboprop Specifications,” Jet Engine. <https://www.jet-engine.net/civtsspec.htm> (accessed Aug. 22, 2023).

[34] A. Kristof, “Energy Losses – Internal Combustion Engines,” Internal Combustion Engines, 2014. <https://sites.lafayette.edu/egrs352-sp14-cars/energy-losses/> (accessed Aug. 22, 2023).

[35] Paragon Scientific, “Certificate of Calibration - Density of Jet Aviation Fuel at 15°C,” LGC Standards. Accessed: Aug. 31, 2023. [Online]. Available: https://assets.lgcstandards.com/system-master%2Fpdfs%2Fh21%2Fh12%2F10542539505694%2FCOA_ALK-CRM-DEKR_ST-WB-CERT-4906345-1-1-1.PDF

[36] A. Horn, “Tight turns,” EngineeringPilot, Sep. 13, 2018. <https://www.engineeringpilot.com/post/2018/09/13/unbenannt> (accessed Aug. 23, 2023).

[37] Airportcodes.io, May 09, 2019. <https://airportcodes.io/en/airport/les-cayes-airport/> (accessed Aug. 23, 2023).

[38] METAR & TAF, “Hinche Airport,” Metar-Taf.com, 2023. <https://metar-taf.com/airport/HT-0003-hinche-airport#runways> (accessed Aug. 24, 2023).

[39] T. Xometry, “All About 7075 Aluminum Alloy,” Xometry, Oct. 24, 2022. Accessed: Sep. 03, 2023. [Online]. Available: <https://www.xometry.com/resources/materials/7075-aluminum-alloy/>

[40] M. Krylov, “Avgas price in Haiti from today #04.09.2023,” Jet A1 Fuel, Aug. 25, 2023. <https://jet-a1-fuel.com/avgas/haiti> (accessed Sep. 04, 2023).

[41] Babu, “Sizing Chart For Clothing,” Babu Baby Clothes. <https://babu.co.nz/content/Sizechartclothing.pdf> (accessed Aug. 06, 2023).

[42] Teledyne FLIR, “Lepton Lens Focal Length,” Jun. 07, 2023. https://flir.custhelp.com/app/answers/detail/a_id/6092/~lepton-lens-focal-length (accessed Aug. 06, 2023).

10.1 Appendix A

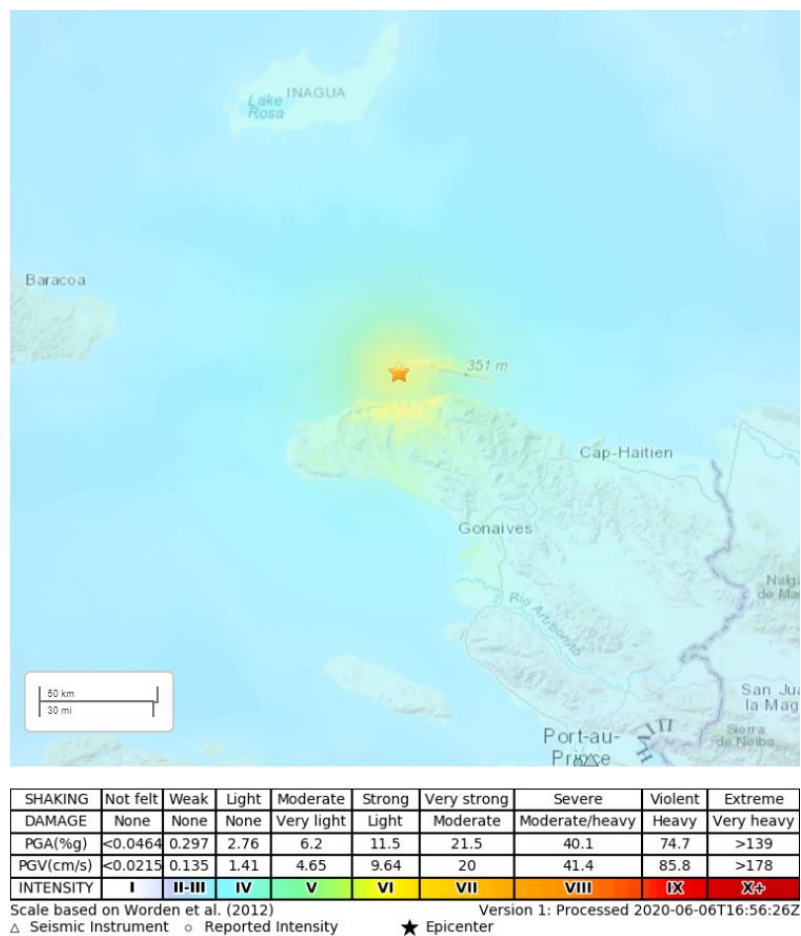


Figure 44 Impact map for the 2018 earthquake used to plot Figure 7

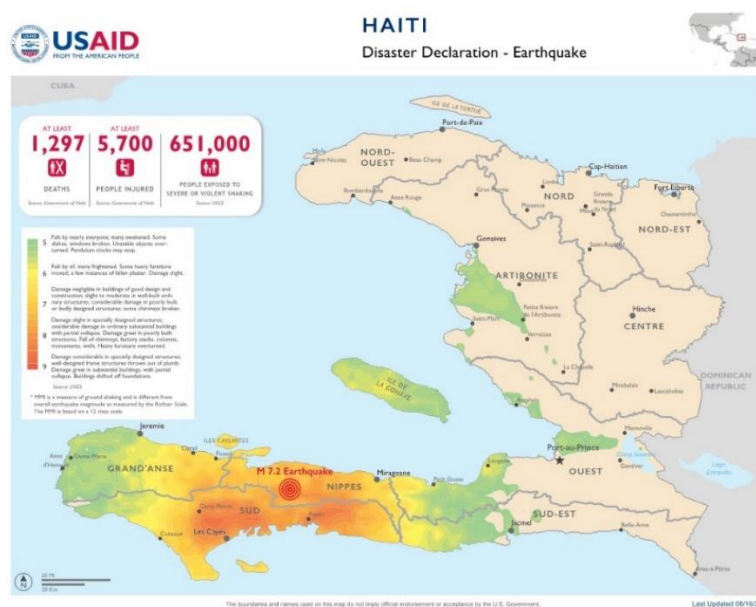


Figure 45 Impact map for the 2021 earthquake used to plot Figure 7

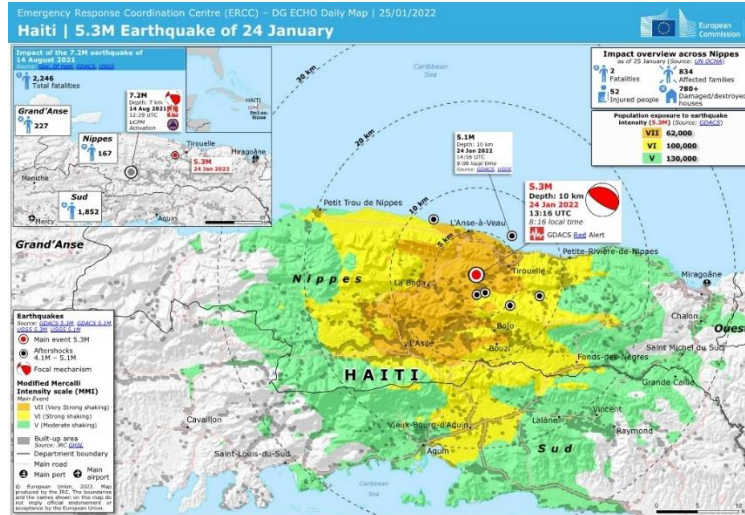


Figure 46 Impact map for the 2022 earthquake used to plot Figure 7

The target critical dimension was based on the average height and shoulder-to-shoulder length of a newborn baby's clothing. Data on a newborn baby's average size was subjective and many sources possessed contradicting data. The height and width (based on the chest measurement) for a newborn baby was 55cm and 20cm, respectively. [41]

The pixel pitch for the FLIR Lepton 3.5 camera was 12 μm [14]. The focal length was 1.77 mm [42]. For the ICI IR Inspector UAV Payload, the pixel pitch was 17 μm [15] and focal length was 35 mm using a 35 mm athermalized focus lens.

Inputs used for equation (7):

$$V_{HT} = 0.672$$

$$S_{HT} = 1.85 \text{ m}^2$$

$$MAC = 0.88 \text{ m}$$

$$S = 6.17 \text{ m}^2$$

Inputs used for equation (8):

$$b = 7.02 \text{ m}$$

$$V_{VT} = 0.0443$$

$$S = 6.17 \text{ m}^2$$

$$L_{VT} = 1.39 \text{ m}$$

Thrust calculations used to plot Figure 31:

The thrust was calculated using:

$$T = \frac{75 * HP * \mu_P}{V}$$

where,

$$HP = 900 \text{ hp}$$

$$\mu_P = 0.8$$

V was varied from 0 to $160 \frac{m}{s}$ while calculating the thrust, T.

Inputs used for equation (9) and equation (10):

$$R = 512.808 \text{ m}$$

$$g = 9.81 \frac{m}{s}$$

$$n = 2.5$$

10.2 Appendix B

Table 12 Data used to plot Figure 13

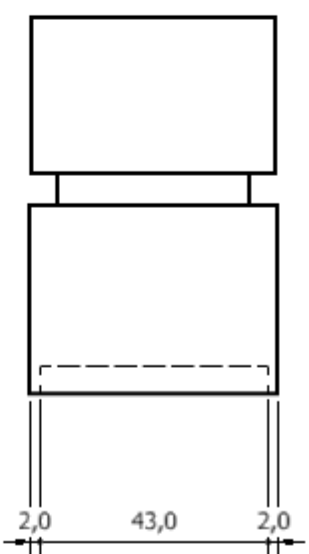
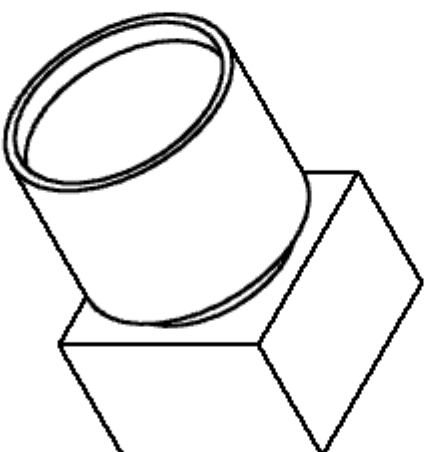
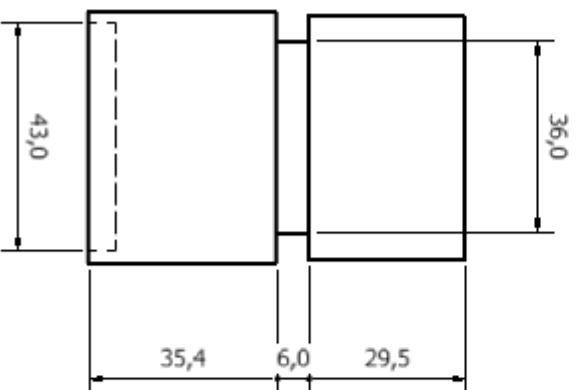
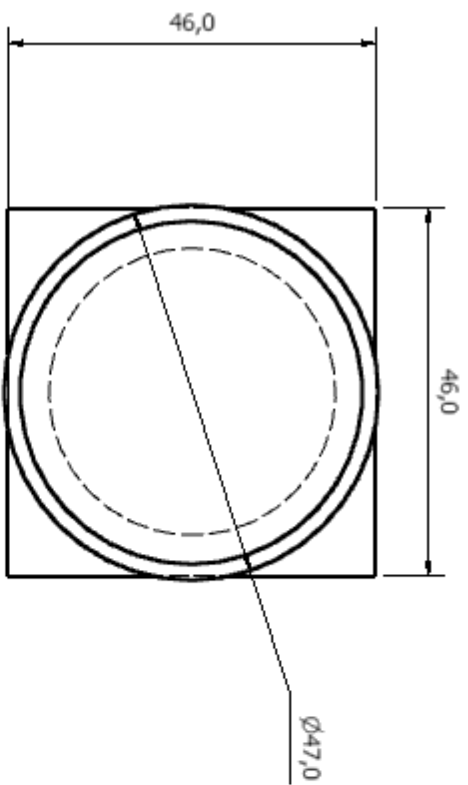
Operating distance [m]	Single image footprint width [m]	Single image footprint height [m]
0	0	0
271	58.861	47.089
542	117.722	94.178
813	176.584	141.267
1084	235.445	188.356
1355	294.306	235.445
1625.98	353.163	282.53

Table 13 Bookkeeping drag table for the design

Component	Length	Sw	t/c	L/D	Q	Re_flight	Re_c/o	Cf	D/q	%
Wing	0.883848	12.33065426	0.09		1.186561	5.63E+06	1.81E+06	0.0038	0.055598	42.34619
HT	0.712612	3.699196279	0.09		1.186561	4.54E+06	1.44E+06	0.004	0.017557	13.37248
VT	0.959803	1.384074284	0.09		1.186561	6.12E+06	1.98E+06	0.0039	0.006405	4.878302
Fuselage	6.078044	12.83798501		5	1.4925	3.87E+07	1.42E+07	0.0027	0.051734	39.40302
								Sum	0.131294	
								86%	0.152668	
								Cdo	0.024762	

10.3 Appendix C

The following pages contain the engineering drawings for the sub-components that made up the integrated design.

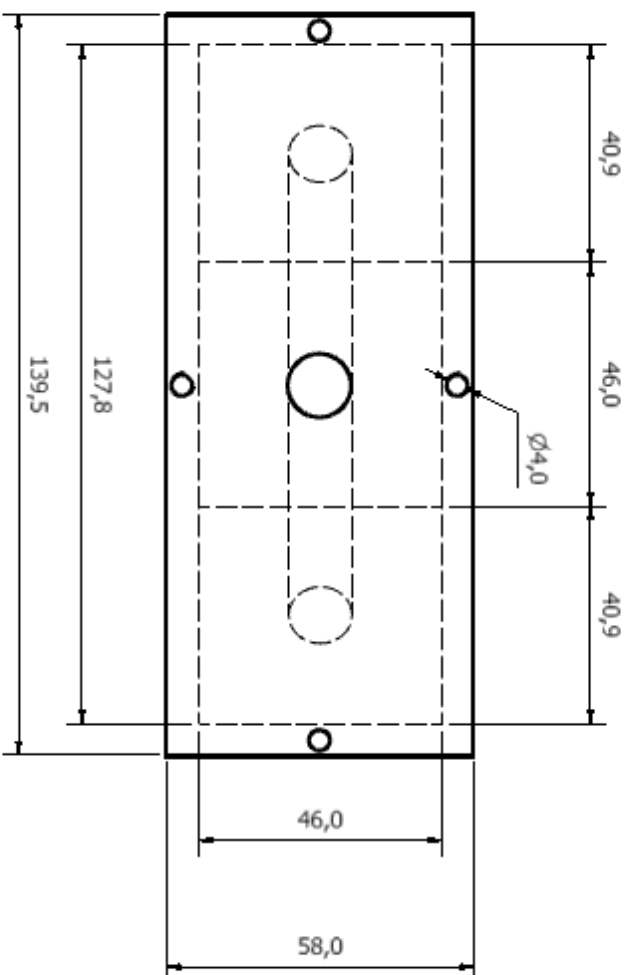
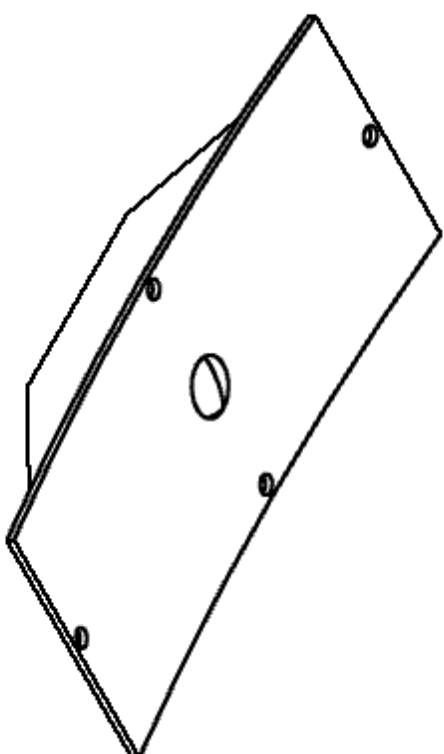
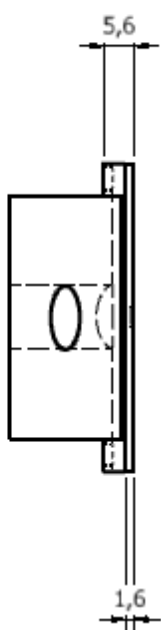
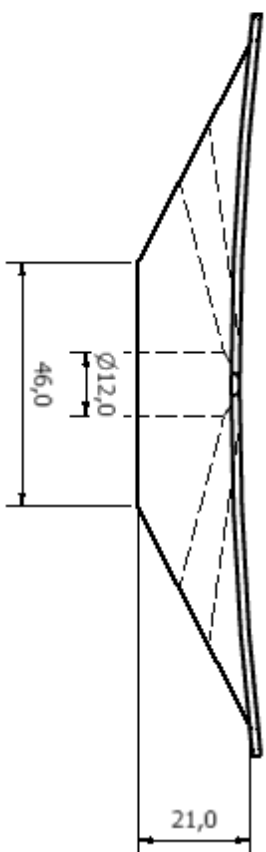


APPROVED:	
DATE: 04/09/2023	
DRAWN BY: Castello	
NOTES:	
SURFACE FINISH	UNLESS
OTHERWISE STATED.	
DIMENSIONS IN mm.	
DO NOT SCALE.	
ALL THREADS MEDIUM FIT.	
ASSEMBLY:	
SCALE: 1:1	
QTY: 3	
DIRG NO:	REV NO.
DESCRIPTION: Camera module with lens	
MATERIAL:	
	SHEET 1 OF 1



SCHOOL OF MECHANICAL, INDUSTRIAL
AND AERONAUTICAL ENGINEERING,
UNIVERSITY OF THE WITWATERSRAND,
JOHANNESBURG.



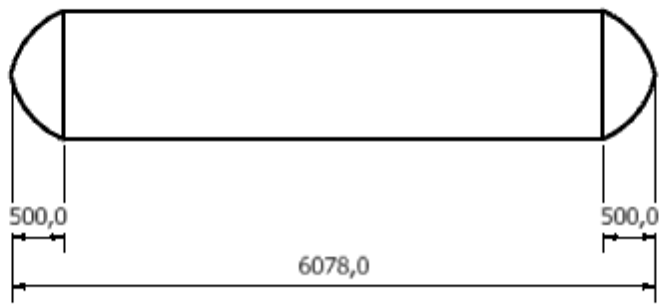
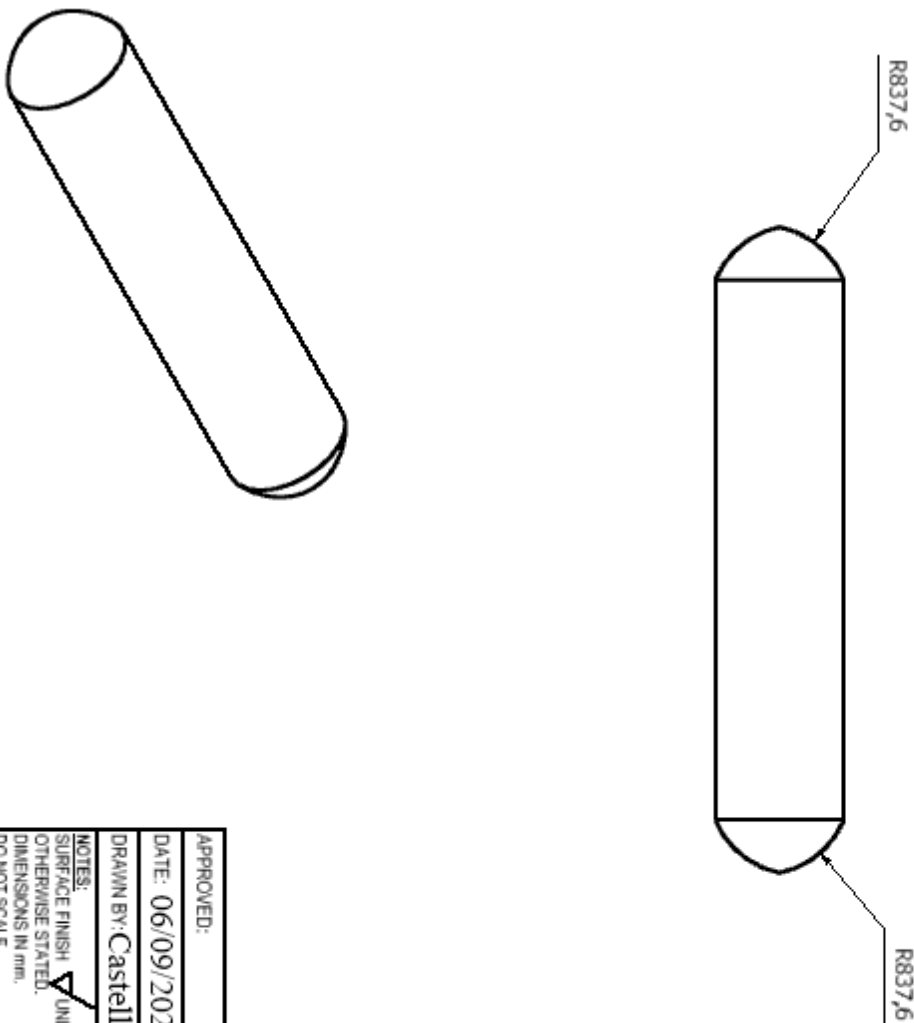
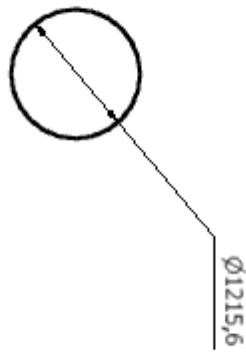



APPROVED:	
DATE: 04/09/2023	
DRAWN BY: Castello	
NOTES:	
SURFACE FINISH	UNLESS
OTHERWISE STATED.	
DIMENSIONS IN mm.	
DO NOT SCALE.	
ALL THREADS MEDIUM FIT.	
ASSEMBLY:	
SCALE: 1:1	
QTY:	
DRG NO:	REV NO:
DESCRIPTION: Mount for cameras to attach to fuselage	
MATERIAL:	



SCHOOL OF MECHANICAL, INDUSTRIAL
AND AERONAUTICAL ENGINEERING,
UNIVERSITY OF THE WITWATERSRAND,
JOHANNESBURG.

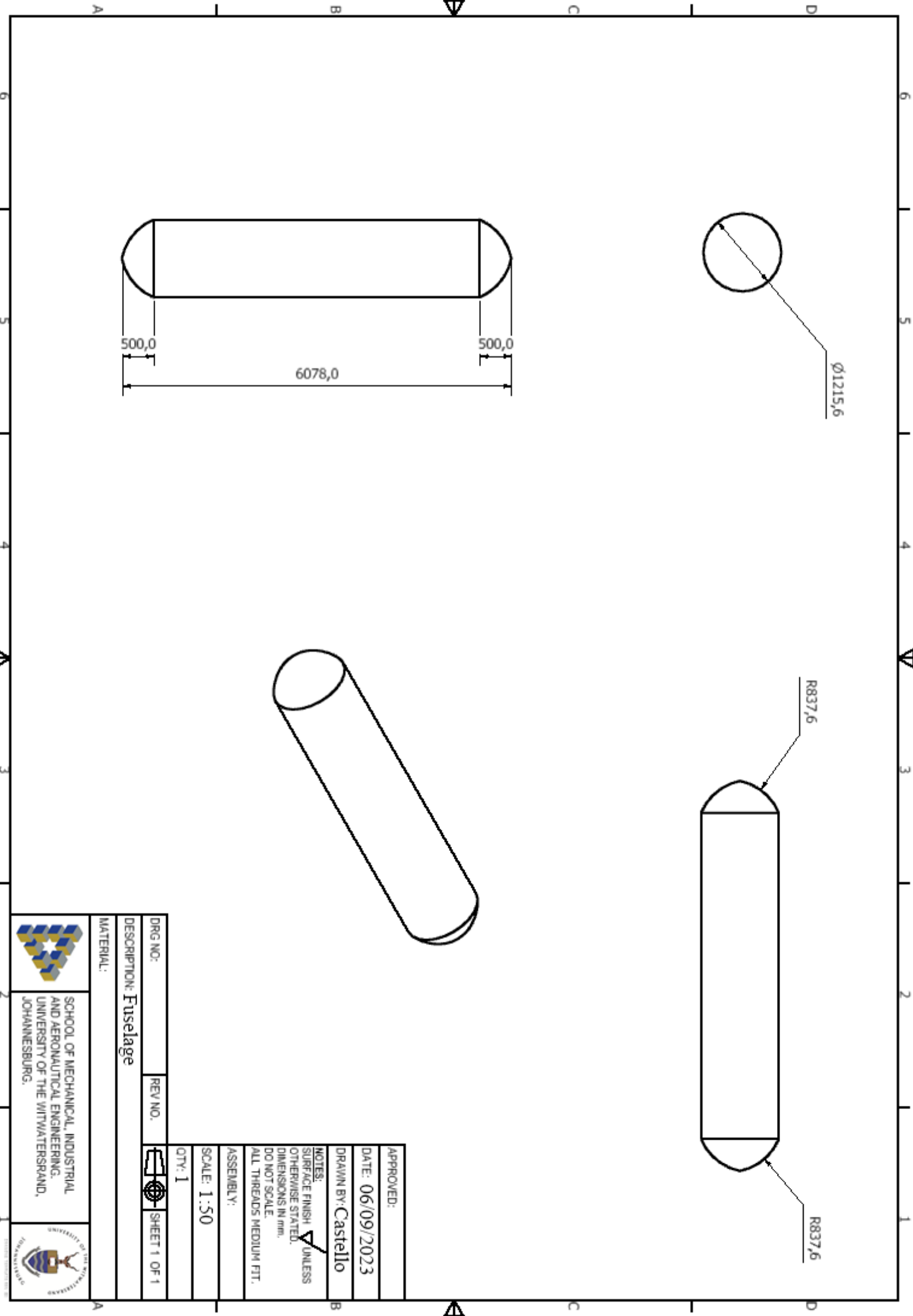


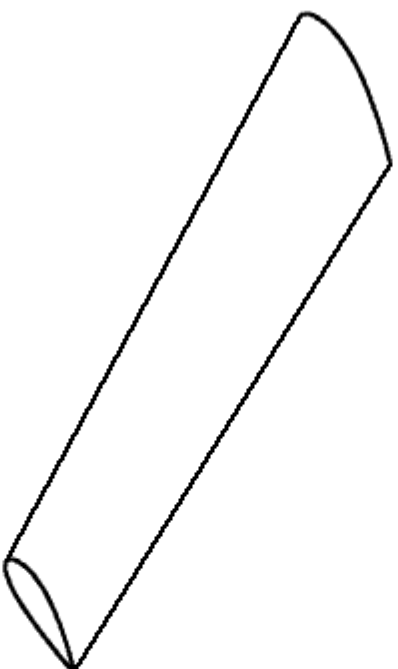
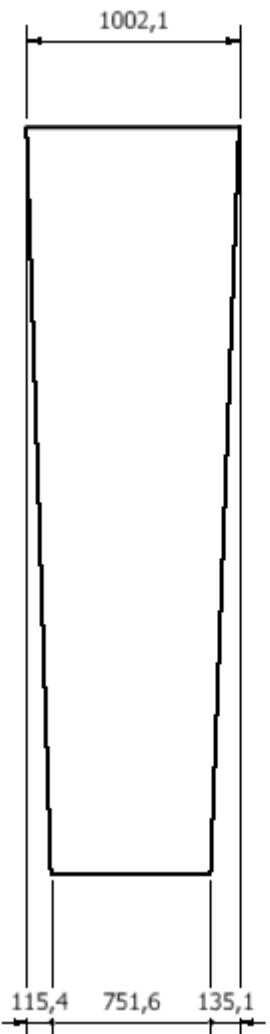
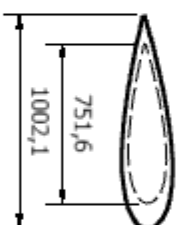
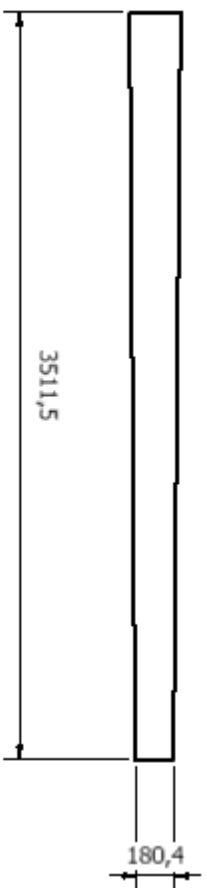


APPROVED:	
DATE: 06/09/2023	
DRAWN BY: Castello	
NOTES: SURFACE FINISH  UNLESS OTHERWISE STATED. DIMENSIONS IN mm. DO NOT SCALE. ALL THREADS MEDIUM FIT.	
ASSEMBLY:	
SCALE: 1:50	
QTY: 1	
DRG NO:	REV NO.
DESCRIPTION: Fuselage	
MATERIAL:	
SHEET 1 OF 1	



SCHOOL OF MECHANICAL, INDUSTRIAL
AND AERONAUTICAL ENGINEERING,
UNIVERSITY OF THE WITWATERSRAND,
JOHANNESBURG.



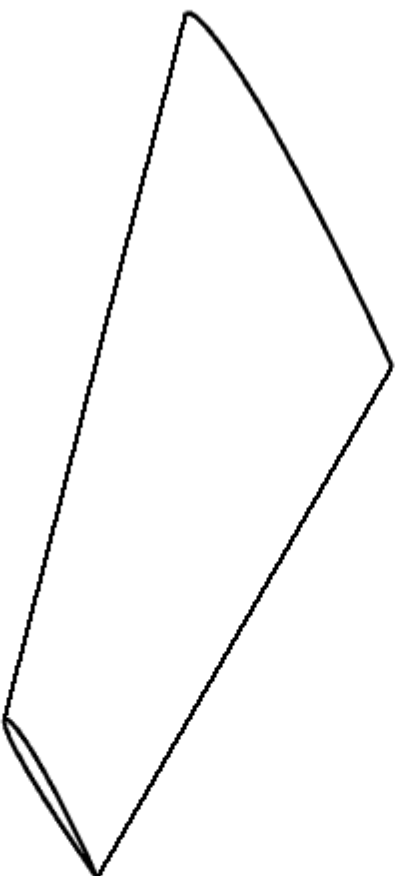
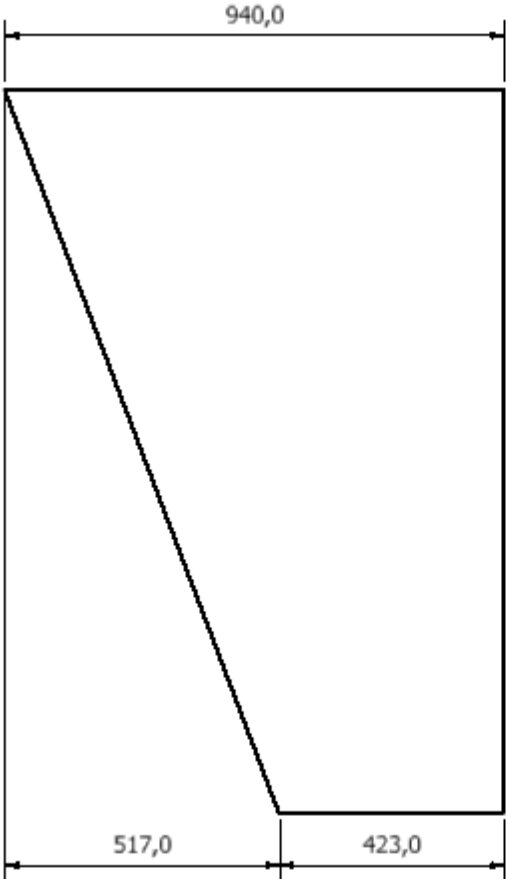
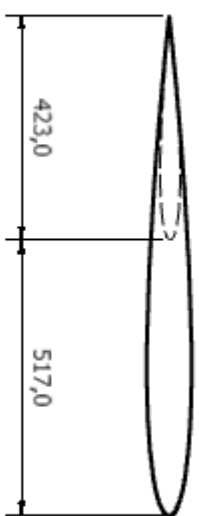
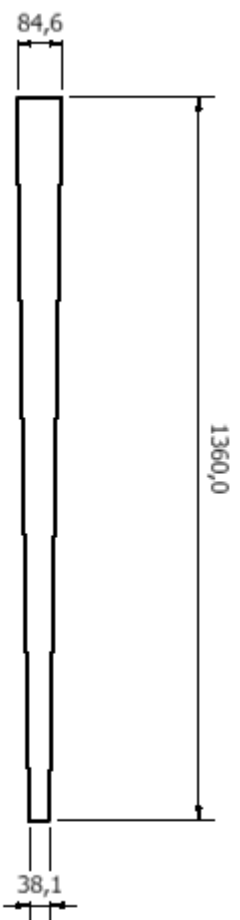


APPROVED:	
DATE: 06/09/2023	
DRAWN BY: Castello	
NOTES:	
SURFACE FINISH	✓ UNLESS OTHERWISE STATED.
DIMENSIONS IN mm.	DO NOT SCALE
ALL THREADS MEDIUM FIT.	
ASSEMBLY:	
SCALE: 1:25	
QTY: 2	
DRG NO:	REV NO.
DESCRIPTION: Wing	
MATERIAL:	



SCHOOL OF MECHANICAL, INDUSTRIAL AND AERONAUTICAL ENGINEERING,
UNIVERSITY OF THE WITWATERSRAND,
JOHANNESBURG.



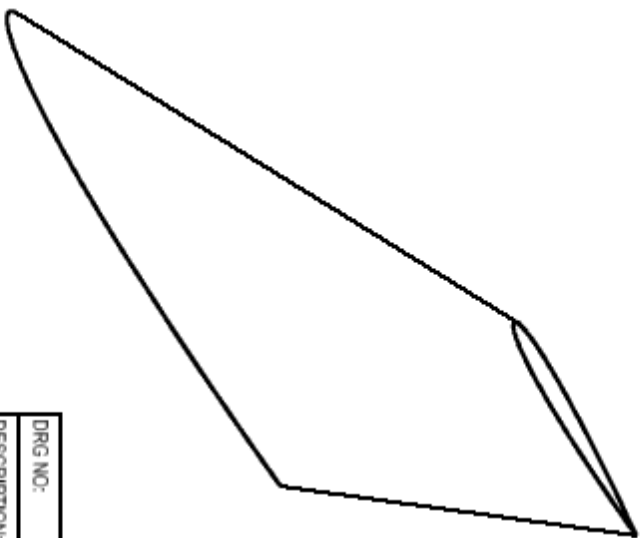
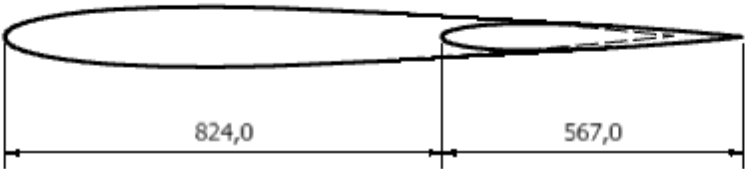
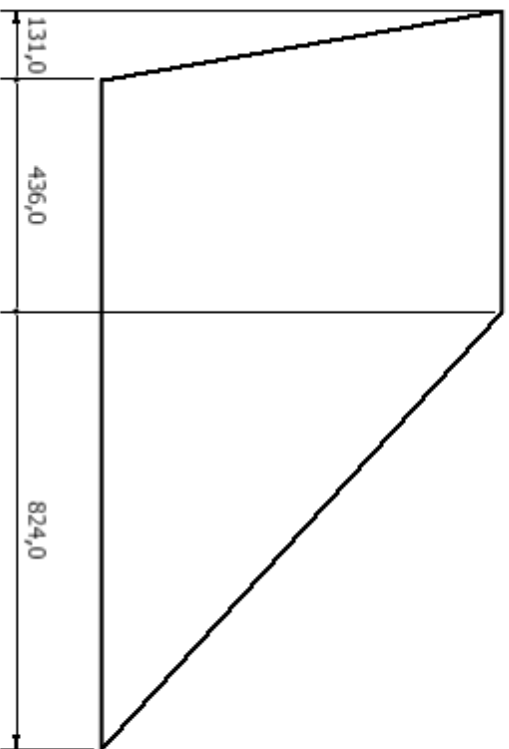
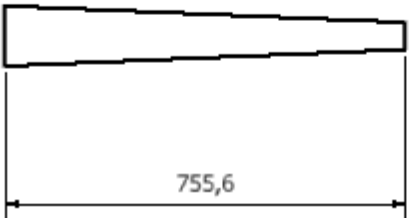


APPROVED:	
DATE: 06/09/2023	
DRAWN BY: Castello	
NOTES:	
SURFACE FINISH: UNLESS OTHERWISE STATED.	
DIMENSIONS IN mm.	
DO NOT SCALE	
ALL THREADS MEDIUM FIT.	
ASSEMBLY:	
SCALE: 1:10	
QTY: 2	
DRG NO.	REV NO.
DESCRIPTION: Horizontal tail	
MATERIAL:	
SHEET 1 OF 1	



SCHOOL OF MECHANICAL, INDUSTRIAL AND AERONAUTICAL ENGINEERING,
UNIVERSITY OF THE WITWATERSRAND,
JOHANNESBURG.





APPROVED:

DATE: 06/09/2023

DRAWN BY: Castello

NOTES:

SURFACE FINISH UNLESS OTHERWISE STATED.

DIMENSIONS IN mm.

DO NOT SCALE.

ALL THREADS MEDIUM FIT.

ASSEMBLY:

SCALE: 1:10

QTY: 1

SHEET 1 OF 1

REV NO.

DRG NO:

DESCRIPTION: Vertical tail

MATERIAL:



SCHOOL OF MECHANICAL, INDUSTRIAL AND AERONAUTICAL ENGINEERING,
UNIVERSITY OF THE WITWATERSRAND,
JOHANNESBURG.

